

# The effects of resolution and noise on kinematic features of fine-scale turbulence

O. R. H. Buxton · S. Laizet · B. Ganapathisubramani

Received: 11 February 2011 / Revised: 10 June 2011 / Accepted: 28 June 2011 / Published online: 14 July 2011  
© Springer-Verlag 2011

**Abstract** The effect of spatial resolution and experimental noise on the kinematic fine-scale features in shear flow turbulence is investigated by means of comparing numerical and experimental data. A direct numerical simulation (DNS) of a nominally two-dimensional planar mixing layer is mean filtered onto a uniform Cartesian grid at four different, progressively coarser, spatial resolutions. Spatial gradients are then calculated using a simple second-order scheme that is commonly used in experimental studies in order to make direct comparisons between the numerical and previously obtained experimental data. As expected, consistent with other studies, it is found that reduction of spatial resolution greatly reduces the frequency of high magnitude velocity gradients and thereby reduces the intermittency of the scalar analogues to strain (dissipation) and rotation (enstrophy). There is also an increase in the distances over which dissipation and enstrophy are spatially coherent in physical space as the resolution is coarsened, although these distances remain a constant number of grid points, suggesting that the data follow the applied filter. This reduction of intermittency is also observed in the eigenvalues of the strain-rate tensor as spatial resolution is

reduced. The quantity with which these eigenvalues is normalised is shown to be extremely important as fine-scale quantities, such as the Kolmogorov length scale, are showed to change with different spatial resolution. This leads to a slight change in the modal values for these eigenvalues when normalised by the local Kolmogorov scale, which is not observed when they are normalised by large-scale, resolution-independent quantities. The interaction between strain and rotation is examined by means of the joint probability density function (*pdf*) between the second and third invariants of the characteristic equation of the velocity gradient tensor,  $Q$  and  $R$  respectively and by the alignments between the eigenvectors of the strain-rate tensor and the vorticity vector. Gaussian noise is shown to increase the divergence error of a dataset and subsequently affect both the  $Q$ – $R$  joint *pdf* and the magnitude of the alignment cosines. The experimental datasets are showed to behave qualitatively similarly to the numerical datasets to which Gaussian noise has been added, confirming the importance of understanding the limitations of coarsely resolved, noisy experimental data.

---

O. R. H. Buxton · S. Laizet · B. Ganapathisubramani  
Department of Aeronautics, Imperial College London,  
London SW7 2AZ, UK

B. Ganapathisubramani  
School of Engineering Sciences, University of Southampton,  
Southampton SO17 1BJ, UK

*Present Address:*

O. R. H. Buxton (✉)  
Center for Aeromechanics Research,  
The University of Texas at Austin,  
Austin, TX 78712-1085, USA  
e-mail: o.buxton@mail.utexas.edu

## 1 Introduction

The last twenty years or so has seen the development of experimental techniques that provide access to all nine components of the velocity gradient tensor,  $D_{ij} = \partial u_i / \partial x_j$ . Wallace and Vukoslavčević (2010) provide a review of studies capable of measuring the full velocity gradient tensor from the use of hot wires to optical techniques such as particle tracking velocimetry (PTV) and particle image velocimetry (PIV). The dynamics of  $D_{ij}$  have provoked great interest since the work of Vieillefosse (1982). This has primarily been driven by the interest in the interaction

between the strain-rate ( $S_{ij}$ ) and rotation ( $\Omega_{ij}$ ) tensors, the symmetric and skew-symmetric components of  $D_{ij}$  respectively. This interaction has been described as “intrinsic to the very nature of three-dimensional turbulence” (Tennekes and Lumley 1972; Bermejo-Moreno et al. 2009). The strain—rotation interaction is a fine-scale feature of turbulent flows, taking place over length scales comparable to the Kolmogorov (dissipative) length scale. Measuring these quantities experimentally is exceedingly challenging as very few three-dimensional experimental studies are capable of resolving these scales, and the examination of under resolved data can skew our understanding of this interaction.

Full three-dimensional velocity fields and the complete velocity gradient tensor can now be obtained through various diagnostic methods. The complete velocity gradient tensor can be obtained at a single point using the multi-point hot-wire technique (Vukoslavčević et al. 1991; Tsinober et al. 1992). The cinematographic stereoscopic PIV studies of Ganapathisubramani et al. (2007, 2008) performed stereo PIV measurements in a plane normal to the streamwise direction and used the Taylor hypothesis to calculate the streamwise components of the velocity gradient tensor (with the other gradients computed in the plane of measurement). Tao et al. (2000, 2002), van der Bos et al. (2002), using holographic PIV, Mullin and Dahm (2006), Ganapathisubramani et al. (2005) using dual-plane stereoscopic PIV, and, Worth (2010), Worth et al. (2010), using tomographic PIV, were able to directly compute all nine components of the velocity gradient tensor without resorting to use of the Taylor hypothesis. Additionally, a three-dimensional particle tracking velocimetry (3D-PTV) technique has been developed by Lüthi et al. (2005), Kinzel et al. (2010) to experimentally measure all the components of the velocity gradient tensor in a Lagrangian way. All of these above-mentioned studies explored the kinematic features of fine-scale turbulence including alignment between the eigenvectors of the strain-rate tensor and the vorticity vector, and the joint probability density functions (*pdfs*) of the invariants of the velocity gradient tensor. Whilst these studies reported qualitatively similar findings, there are some quantitative differences in, for example, the peak values of the strain—rotation alignment *pdfs*. This is perhaps attributable to different spatial resolution achieved in these techniques and/or the experimental noise present in the data. It is thus extremely important to determine the effect that spatial resolution and experimental noise play in observing the physics of the strain—rotation interaction. This interaction is inherently multi-scale in nature, and some aspects of it will not be observable at coarser resolutions, thereby distorting our understanding of the physical processes that underpin it.

Previous work on the resolution effects of measurement of fine-scale turbulence has shown that coarsely resolved data underestimates magnitudes of the velocity gradients (Antonia et al. 1994) and quantities such as enstrophy ( $\omega_i^2$ ) and dissipation ( $\epsilon = 2\nu S_{ij}S_{ij}$ ), the scalar counterparts to rotation and strain-rate respectively, that are derived from the velocity gradient tensor (Lavoie et al. 2007). The turbulent channel flow study of Antonia et al. (1994), for example, shows that as resolution is coarsened to  $5\eta$  the ratio of the measured component  $\langle (\partial u_1 / \partial x_1)^2 \rangle$  to the “actual value” can fall away to 0.75 at a  $y^+$  of 40. More coarsely resolved data also does not tend to “pick up” the extreme events, several thousand times the mean (Donzis et al. 2008), that is so important in fine-scale turbulence (Tsinober 1998). Coarsely resolved data has also been shown to increase the physical length scales over which  $\omega_i^2$  and  $\epsilon$  are spatially coherent (Worth 2010). In addition to the problem of limited resolution, experimental studies suffer from the presence of experimental noise, in particular on the velocity gradients. Christensen and Adrian (2002) describe the three main sources of noise on PIV velocity fields as being random error due to electrical noise within the camera, bias error due to pixel peak locking etc. and gradient noise due to local random velocity gradients within the flow. Additionally, there is a noise floor associated to the sub-pixel interpolation in the PIV processing algorithm which equates to 0.06 pixels for a  $32 \times 32$  pixel interrogation window Herpin et al. (2008). These errors are further discussed in Westerweel (2000). Although methods can be found to ameliorate some of these errors, such as pixel peak locking (Christensen 2004), they can never be completely eliminated. The effect of experimental noise is investigated by Lund and Rogers (1994). They show that qualitatively similar results can be found when comparing probability density functions (*pdfs*) formed from the hot wire data of Tsinober et al. (1992) and their DNS results to which Gaussian noise has been added. They state that the divergence error introduced into the data as a result of this noise is of great significance to *pdfs* of quantities such as the eigenvalues of the rate of strain tensor.

Given that advanced techniques aim to capture kinematics and dynamics of fine-scale turbulence, it is essential that we understand the effects of resolution and noise on our observations and conclusions. This study, therefore, sets out to examine the effects of spatial resolution and experimental noise on the observation of the velocity gradient tensor, and its kinematic features in fine-scale turbulence. First, the effect of resolution is examined using data from the self-similar region of a direct numerical simulation (DNS) of a nominally two-dimensional planar mixing layer that is filtered at four different spatial resolutions and compared to the “best case” original dataset.

Second, the effect of noise on the kinematics of fine-scale turbulence is explored by adding zero mean Gaussian noise to the four mean filtered datasets. This data are then compared against experimental data, which comes from Ganapathisubramani et al. (2007), taken in the far field of a turbulent axisymmetric jet. It will thus present the effects of coarsening spatial resolution and experimental noise on the velocity gradients and explore how this influences the observation of strain and rotation, which is crucial in furthering the experimental observation of the strain–rotation interaction.

## 2 Experimental and numerical methods

This study relies upon experimental data from the far field of an axisymmetric turbulent jet and data from a direct numerical simulation of a nominally two-dimensional planar mixing layer.

### 2.1 Experimental methods

The data used in this study were obtained by Ganapathisubramani et al. (2007). The study examined the turbulence in the far field of an axisymmetric turbulent jet which exhausted into a mild co-flow of air from a pipe of circular cross-section of diameter 26 mm.

Cinematographic stereoscopic PIV measurements were performed in the “end view” plane ( $x_2 - x_3$ ) at a downstream axial location of  $x_1 = 32$  pipe diameters. Further details regarding the experimental techniques are available in Ganapathisubramani et al. (2007). The relevant length scales at the measurement location were: jet half-width ( $\delta_{1/2}$ ) = 126 mm, Taylor microscale ( $\lambda$ ) = 13.8 mm, Kolmogorov length scale ( $\eta$ ) = 0.45 mm. The Kolmogorov length scale is defined as  $\eta = (v^3/\langle\epsilon\rangle)^{1/4}$ , where  $\langle\epsilon\rangle$  is the mean rate of dissipation which is calculated directly from the experimental data and the Reynolds number based on Taylor microscale is  $Re_\lambda \approx 150$ . Evidently, there is no better estimate for the Kolmogorov length scale than that calculated directly from the mean dissipation rate of the dataset and hence, unless otherwise stated, this will be regarded as  $\eta$  for the experimental data as opposed to  $\eta_i$ , i.e. the “local” Kolmogorov length scale.

The resolution of the stereoscopic vector fields is approximately  $3\eta \times 3\eta$  (1.35 mm  $\times$  1.35 mm) and successive vectors are separated by  $1.5\eta$  due to the 50% oversampling. The total field size is  $160\eta \times 160\eta$  (76 mm  $\times$  76 mm). Taylor’s hypothesis with a convection velocity equal to the local mean axial velocity,  $\langle\mathbf{u}_1\rangle(x_2, x_3)$ , was utilised to reconstruct a quasi-instantaneous space-time volume. This data were then filtered with a Gaussian

filter of filter width  $3\eta$  in all three directions in order to reduce the spatial velocity gradients’ noise levels. These spatial gradients were calculated with a second-order central difference scheme. Due to intrinsic uncertainties associated with performing stereoscopic PIV measurements, the velocity field was not divergence free (i.e.  $\nabla \cdot \mathbf{u} \neq 0$ ). The divergence error is in line with other experimental studies and is characterised and discussed further in Ganapathisubramani et al. (2007).

### 2.2 Numerical methods

Direct numerical simulations of a nominally two-dimensional planar mixing layer, generated by means of two flows of different freestream velocities ( $U_1$  and  $U_2$ ) either side of a splitter plate of thickness  $h$  were performed. The computational domain ( $L_x \times L_y \times L_z$ ) = (230.4h  $\times$  48h  $\times$  28.8h) is discretised on a Cartesian mesh (stretched in the cross-stream direction) of  $(n_x \times n_y \times n_z)$  = (2,049  $\times$  513  $\times$  256) mesh nodes. The stretching of the mesh in the cross-stream direction leads to a minimal mesh size of  $\Delta y_{\min} \approx 0.03h$ . The time step,  $\Delta t = 0.05h/U_c$ , where  $U_c = (U_1 + U_2)/2$  is the mean convection velocity, is low enough to satisfy the Courant-Friedrichs-Lewy (CFL) condition, ensuring the temporal stability of the solution. It is a necessary condition for convergence of finite difference schemes when solving the Navier-Stokes equations. The Reynolds number,  $Re_w$ , based on  $U_c$  and  $h$  is 1000 and the Reynolds number based on Taylor microscale, computed assuming isotropic turbulence (Taylor 1935), is  $Re_\lambda \approx 180$ .

The boundary layers of thicknesses (corresponding to  $\delta_{99}$ )  $\delta_1 = 4h$  and  $\delta_2 = 3h$  are laminar with a Blasius profile imposed at the inlet. They are submitted to residual 3D perturbations allowing a realistic destabilisation of the flow downstream of the trailing edge. The spectral content of this artificial perturbation is imposed to avoid the excitation of high wave numbers or frequency waves that cannot be correctly described by the computational mesh. More details about the generation of the inlet/initial conditions can be found in Laizet et al. (2010).

An in-house code (called “Incompact3d”) based on sixth-order compact schemes for spatial discretisation and second-order Adams-Bashforth scheme for time advancement is used to solve the incompressible Navier-Stokes equations. To treat the incompressibility condition, a projection method is used, requiring the solution of a Poisson equation for the pressure. This equation is fully solved in spectral space via the use of the relevant three-dimensional fast Fourier transforms (FFT) that allows the consideration of all the combinations of free-slip, periodic or Dirichlet boundary conditions on the velocity field in the three spatial directions. In the present calculations, the boundary conditions are only inflow/outflow in the

streamwise direction (velocity boundary conditions of the Dirichlet type), free slip in the cross-stream direction at  $y = -L_y/2$  and  $L_y/2$  and periodic in the spanwise direction at  $z = -L_z/2$  and  $L_z/2$ . The pressure mesh is staggered from the velocity mesh to avoid spurious pressure oscillations. Using the concept of modified wavenumber, the divergence-free condition is ensured up to the machine accuracy. More details about the present code and its validation, especially the original treatment of the pressure in spectral space, can be found in Laizet and Lamballais (2009).

### 2.3 Varying the resolution and computing spatial velocity gradients

A section of the computational domain, 301 mesh nodes in streamwise extent just upstream of the streamwise extent of the domain, was isolated. Three snapshots of this domain were saved at a sufficient number of time steps apart to ensure that all three realisations were statistically independent. This region of the flow was shown to be in the self-similar region, meaning that fair comparisons between the computational and experimental data could be made. A reference case was generated by calculating the spatial velocity derivatives of this reduced domain using a modified version of the sixth-order scheme. This reference case is thus the “best case” of highest spatial resolution and highest-order accurate numerical scheme on the existing stretched grid. The reference case was then mean filtered onto uniform Cartesian grids (including in the cross-stream direction in which the original mesh was stretched) at four different resolutions, namely  $\Delta x$ ,  $2\Delta x$ ,  $3\Delta x$  and  $6\Delta x$  (2.5, 5, 7.5 and  $15\eta$ , where  $\eta$  is the Kolmogorov length scale calculated from the reference case). The data were then oversampled with a 50% overlap such that the grid spacing was half the spatial resolution, in order to best mimic typical PIV experiments. Spatial velocity gradients were then calculated for these four

differently resolved data sets using second-order central differencing, i.e.

$$\left. \frac{\partial u}{\partial x} \right|_x = \frac{u(x + \Delta g) - u(x - \Delta g)}{2\Delta g} + O(\Delta g^2) \quad (1)$$

where  $\Delta g$  is the grid spacing, which is half of the spatial resolution. It is possible to improve the accuracy of the gradients by oversampling at a higher rate, although when this oversampling is too large the gradients become extremely noisy, or by using a higher-order stencil to calculate the gradients. However, our choice of grid spacing (i.e. 50% overlap) and finite difference scheme (second-order accurate central difference) is chosen to match most PIV studies in the literature (Tao et al. 2000, 2002; Ganapathisubramani et al. 2005; Worth et al. 2010).

Table 1 summarises the flow quantities for the reference case DNS and all four mean filtered numerical datasets from which the gradients are calculated using the second-order scheme of equation 1. It can thus be observed that the dataset mean filtered at  $15\eta$  has a spatial resolution of  $\approx 10\eta$ , or ten times the “local” Kolmogorov length scale (which is the dissipative length scale directly computed from the coarsely resolved dataset itself), which is typical of the resolution of the large-scale component of Kinzel et al. (2010) and the study of Ganapathisubramani et al. (2005).

The study of Lavoie et al. (2007) used the assumption of local isotropy to estimate the mean rate of dissipation in freely decaying turbulence behind a grid such that:

$$\langle \epsilon \rangle_{\text{iso}} \approx 15\nu \left\langle \left( \frac{\partial u_1}{\partial x_1} \right)^2 \right\rangle \quad (2)$$

The “local” Kolmogorov length scale, shown in Table 1, is computed from the mean rate of dissipation directly calculated from the mean filtered datasets using all nine components of the velocity gradient tensor and without recourse to the approximation of local isotropy. It can be shown that:

**Table 1** Summary of mean rate of dissipation ( $\langle \epsilon \rangle$ ), “local” Kolmogorov scale ( $\eta$ ), r.m.s. streamwise velocity fluctuation ( $\sqrt{\langle u_1'^2 \rangle}$ ), Taylor microscale ( $\lambda$ ) and Reynolds number based on

	Reference case DNS	$2.5\eta$	$5\eta$	$7.5\eta$	$15\eta$
$\Delta g/\eta$	–	1.25	2.5	3.75	7.5
$\langle \epsilon \rangle / (U_c^3/h)$	$2.45 \times 10^{-4}$	$2.05 \times 10^{-4}$	$1.21 \times 10^{-4}$	$8.12 \times 10^{-5}$	$4.41 \times 10^{-5}$
$\eta/h$	0.0449	0.0470	0.0537	0.0592	0.0690
$\eta/\eta$	1	1.05	1.19	1.32	1.54
$\sqrt{\langle u_1'^2 \rangle} / U_c$	0.151	0.152	0.145	0.144	0.143
$\lambda/h$	1.18	1.31	1.61	1.95	2.62
$Re_\lambda \approx$	180	200	230	280	370

Taylor microscale ( $Re_\lambda$ ) for differently resolved numerical datasets in terms of splitter plate thickness ( $h$ ) and convection velocity ( $U_c = (U_1 + U_2)/2$ )

$$\frac{\langle \epsilon_l \rangle}{\langle \epsilon \rangle} \sim \left( \frac{\eta_l}{\eta} \right)^{-4} \quad (3)$$

Lavoie et al. (2007) show that their estimates for dissipation using uncorrected PIV data of resolution  $11\text{--}14\eta$  varies between  $\approx 0.2\text{--}0.3$  times their best estimate of dissipation using the assumption of local isotropy. This compares extremely well with the “local” Kolmogorov length scale data in Table 1 which would suggest that the estimates for  $\langle \epsilon_l \rangle$  will vary between 0.33 and 0.18 times the mean dissipation rate from the reference case DNS as resolution is coarsened from  $7.5\eta$  to  $15\eta$ . This suggests that the qualitative and quantitative findings of this study are comparable to other turbulent flows such as freely decaying grid turbulence.

The experimental data were split into time series that encompassed a change in streamwise coordinate ( $x_1$ ) of approximately  $150\eta$ , which is comparable to the extent of the domain in both directions of the azimuthal plane ( $x_2 - x_3$ ). These time series were used to construct pseudo-volumes of data by means of the Taylor hypothesis and using a convection velocity equal to the local mean streamwise velocity, i.e.  $\langle u_1 \rangle(x_2, x_3)$  (Ganapathisubramani et al. 2007). These pseudo-volumes were then mean filtered in the same way as the numerical domain, at a resolution of  $6\eta$ , and spatial gradients were again calculated using the second-order accurate scheme of Eq. 1. Direct comparisons could thus be made between the numerical data, at the various resolutions, and the experimental data at both resolutions with all of the gradients being second-order accurate.

### 3 Results and discussion

#### 3.1 Effects of spatial resolution

Figure 1 shows probability density functions (*pdfs*) for the diagonal components of the velocity gradient tensor for the reference DNS case (a) and the mean filtered datasets (b)–(e). All of the *pdfs* are normalised by the Kolmogorov length scale calculated from the reference case DNS, i.e. the best estimate of  $\eta$  for the true flow. The tails of the *pdfs* become successively narrower as the resolution is reduced (a)–(e). This reflects the reduction in frequency in the intermittent, high magnitude velocity gradient events as spatial resolution is coarsened. This effect can also be observed in the narrowing of the tails of Fig. 2a–e, which show the *pdfs* for the non-diagonal components of the velocity gradient tensor at the various resolutions.

The *pdfs* of the diagonal components of Fig. 1 show a negative skewness, which is more pronounced at the highest resolutions, e.g. Fig. 1a, than for the lower resolutions. This negative skewness is in agreement with the experimental

study of Mullin and Dahm (2006), which observed the turbulence in the far field of a turbulent jet. Skewness decreases with decreasing resolution (i.e. coarseness). For example, the skewness of  $\partial u_1 / \partial x_1$  reduces from  $-0.44$  in the reference DNS case to  $-0.19$  at  $15\eta$  resolution.

Mullin and Dahm (2006) described the straight line decay in semi-logarithmic axes of the velocity gradient *pdfs*. These exponential tails can be seen in the more coarsely resolved *pdfs* of Figs. 1c–e and 2c–e, but are not present in the reference DNS cases and most finely mean filtered datasets of Figs. 1, 2a, b. These non-exponential tails are most clearly visible for the non-diagonal components of  $D_{ij}$  in Fig. 2, and show a decreasing slope of the *pdf* tails, particularly so for the negative (left) tails.

Figure 3 shows *pdfs* for dissipation, (a) and (c), and enstrophy, (b) and (d). Figure 3a, b are produced from the numerical datasets and (c) and (d) are produced from the experimental datasets. It can be seen that as the resolution is decreased the tails of both the dissipation and enstrophy *pdfs* are greatly narrowed, indicating a reduction of “extreme events” of exceptionally high dissipation/enstrophy. The “extreme events” of strong local strain–rotation interaction have been shown to be dynamically extremely important in the role of enstrophy amplification (Ruetsch and Maxey 1991; Tsinober et al. 1992; Vincent and Meneguzzi 1994; Tsinober 1998). Buxton and Ganapathisubramani (2010) showed that a small proportion of the flow, encompassing these “extreme events”, was responsible for a much larger proportion of the overall enstrophy amplification. The original experimental data were Gaussian filtered at a filter width of  $3\eta$  and can be observed to fall between the first two mean filtered DNS datasets (at  $2.5$  and  $5\eta$ ), by comparing figures (a) and (c), and (b) and (d). The reduction in intermittency, and therefore frequency of extreme events, can be seen to occur for both the numerical and experimental data. The *pdfs* for dissipation and enstrophy appear to show a similar narrowing as resolution is coarsened (both numerically and experimentally), suggesting that strain-dominated regions of the flow are almost equally sensitive to spatial resolution as rotationally dominated regions.

Figures 4 and 5 illustrate the distances over which dissipation ( $\epsilon$ ) and enstrophy ( $\omega_i^2$ ) are spatially coherent. One-dimensional traces, along the streamwise direction, were produced from the numerical domains of various resolutions. High dissipation/enstrophy events were then identified as a function of the global maxima for dissipation ( $\epsilon > 0.01\epsilon_{\max}$ ) and enstrophy ( $\omega_i^2 > 0.01(\omega_i^2)_{\max}$ ). Local maxima ( $\epsilon|_{\max}$ ), ( $\omega_i^2|_{\max}$ ) for each event were then found and a distance, linearly interpolated between successive grid points, was identified between crossing points of  $e^{-1} \cdot \epsilon|_{\max}$  or  $e^{-1} \cdot \omega_i^2|_{\max}$ . A probability density function of

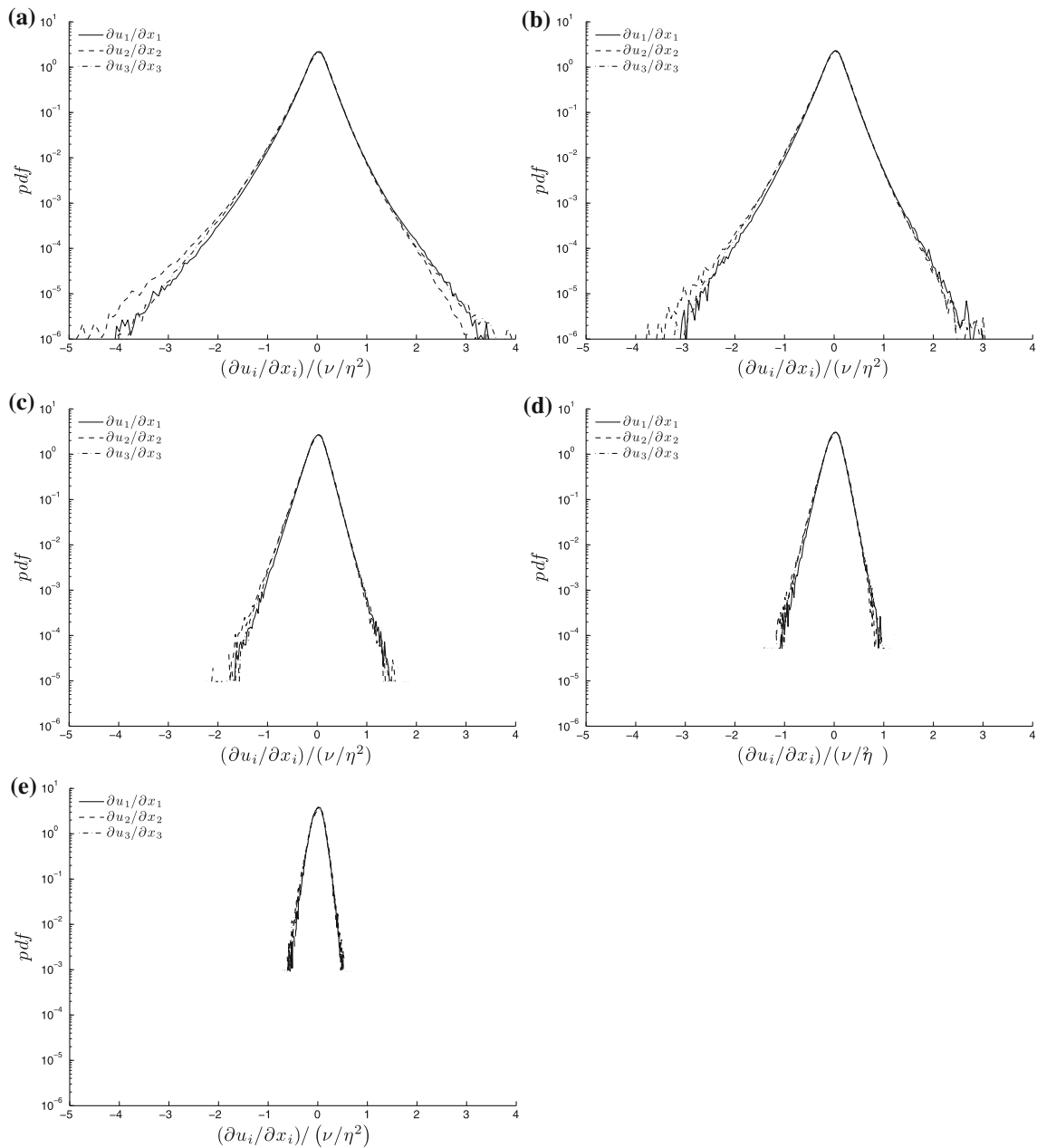


**Fig. 1** Probability density functions for the normalised diagonal components of the velocity gradient tensor for (a) the reference DNS dataset, (b) the dataset mean filtered at  $2.5\eta$ , (c) the dataset mean filtered at  $5\eta$ , (d) the dataset mean filtered at  $7.5\eta$  and (e) the dataset mean filtered at  $15\eta$

this distance,  $r_\epsilon$  or  $r_{\omega_i^2}$ , was then compiled for all of the high dissipation/entrophy events along all the streamwise traces and presented in Figs. 4 and 5.

Similar *pdfs* were produced from one-dimensional traces in the other directions ( $x_2$  and  $x_3$ ). Although not shown for brevity, they are qualitatively and quantitatively virtually identical to the figures presented here, in the streamwise direction.

It should be noted that the peaks for the *pdfs* based upon grid points for both dissipation and entrophy, Fig. 4a, b

respectively, occur at the same value for all four resolutions—approximately 3.4 grid points for dissipation and 2.4 grid points for entrophy. This finding illustrates the fact that the characteristic length scale of structures of high dissipation and entrophy follow the imposed filter. This means that the observation of these extreme events will be dictated by the spatial resolution of the experiment designed to observe them. The fact that the characteristic “diameter” of these structures remains a constant number of grid points, thereby following the imposed filter, as the

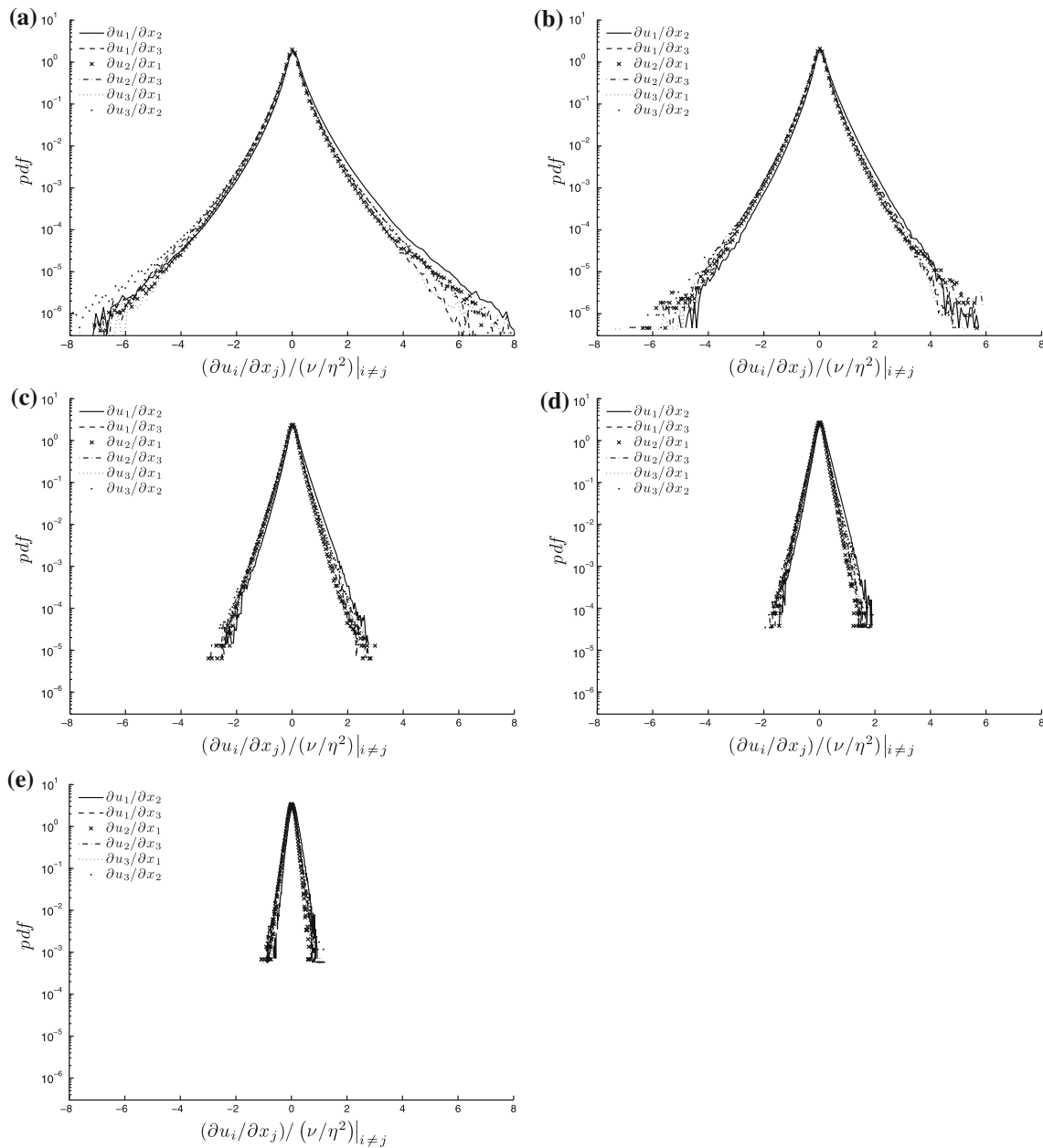


**Fig. 2** Probability density functions for the normalised non-diagonal components of the velocity gradient tensor for (a) the reference DNS dataset, (b) the dataset mean filtered at  $2.5\eta$ , (c) the dataset mean

filtered at  $5\eta$ , (d) the dataset mean filtered at  $7.5\eta$  and (e) the dataset mean filtered at  $15\eta$

resolution changes is in agreement with the tomographic PIV study of Worth (2010). In physical space, however, Fig. 5a, b show that as resolution becomes coarser these characteristic length scales increase. The pdfs for these two figures are normalised by  $\eta$  calculated from the best case DNS dataset and is thus representative of the best approximation to  $\eta$  for the true flow.

Figure 5c, d, showing the characteristic length scales for dissipation and enstrophy respectively, are normalised by the “local” Kolmogorov length scale, i.e. that calculated

from the dataset from which the pdf is produced and summarised in Table 1. This is representative of the Kolmogorov length scale that will be calculated from experimental data at a given resolution. Although the Kolmogorov length scale increases as resolution is coarsened, as a consequence of the mean rate of dissipation reducing (c.f. Fig. 3), this reduction does not match the characteristic length scale of these “extreme events” remaining a constant number of grid points. Thus, Fig. 5c, d also show the distances over which dissipation and

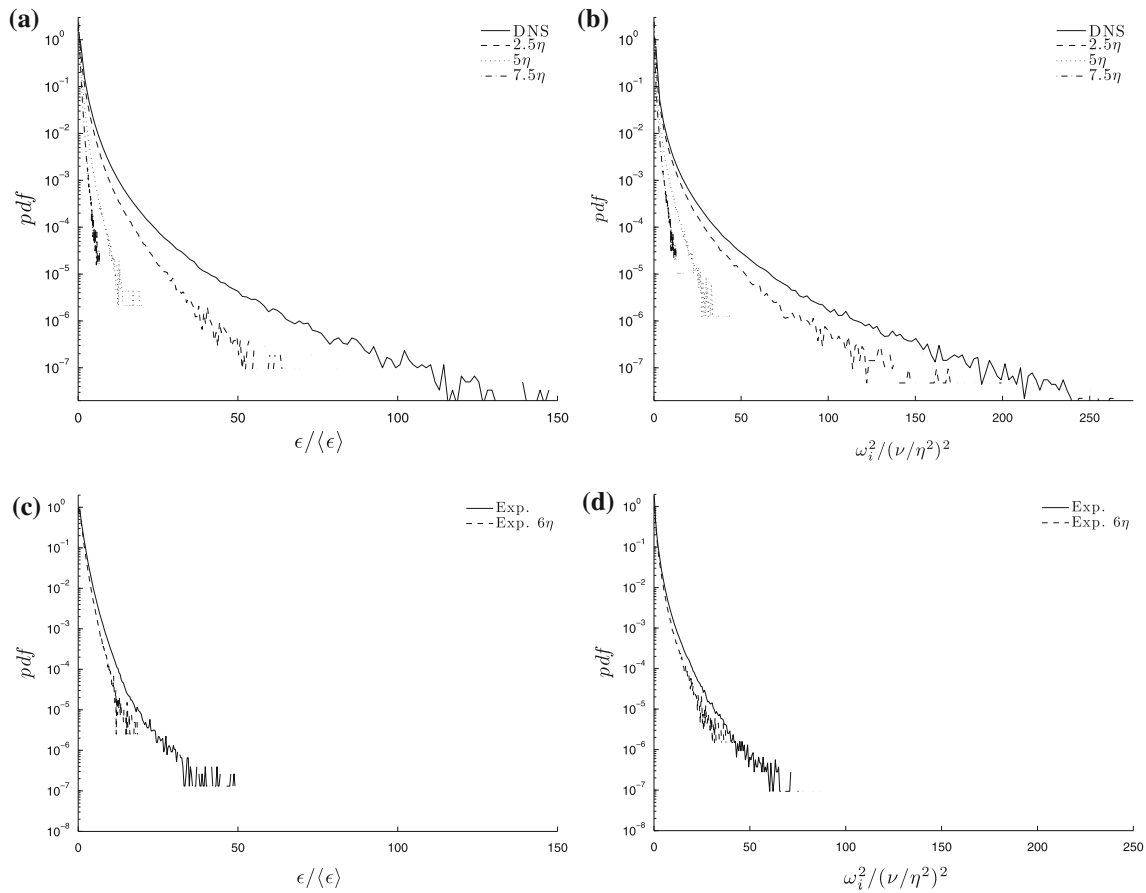


**Fig. 3** **a** Probability density function of dissipation normalised by the mean dissipation rate from the reference case,  $\langle \epsilon \rangle$  from the numerical data. **b** *pdf* of normalised enstrophy from the numerical data. **c** *pdf* of

normalised dissipation from the experimental data. **d** *pdf* of normalised enstrophy from the experimental data

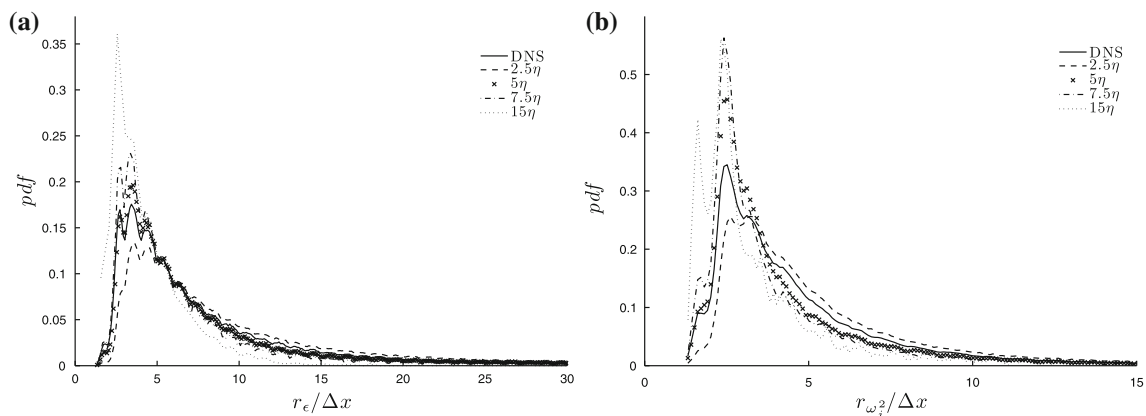


**Fig. 4** **a** Probability density function of “diameter” of high dissipation events in the streamwise ( $x_1$ ) direction in terms of grid points ( $\Delta x$ ). **b** *pdf* of “diameter” of high enstrophy events in the streamwise direction in terms of  $\Delta x$

enstrophy are spatially coherent increase in physical space as resolution is coarsened, although to a lesser extent than when compared to the true flow’s dissipative length scale illustrated in Fig. 5a, b. This has important consequence for

coarsely resolved experimental data from which fine-scale quantities, such as  $\eta_l$  have to be computed directly.

Due to the fact that the one-dimensional traces may intersect the high dissipation/enstrophy event at any

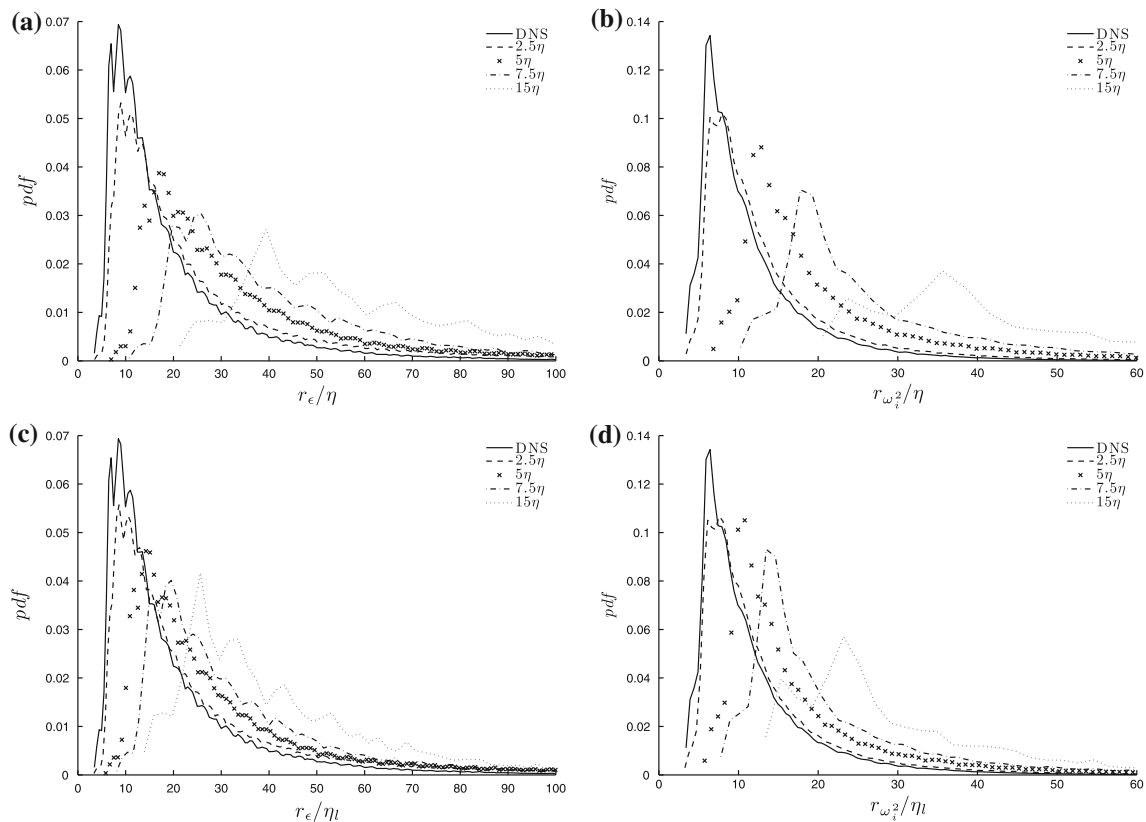


**Fig. 5** (a) Probability density function of “diameter” of high dissipation events in the streamwise ( $x_1$ ) direction in terms of the Kolmogorov length scale calculated from the reference case DNS ( $\eta$ ). (b) *pdf* of “diameter” of high enstrophy events in the streamwise direction in terms of  $\eta$ . (c) *pdf* of “diameter” of high dissipation

events in the streamwise direction in terms of the “local” Kolmogorov length scale, calculated from the mean filtered datasets ( $\eta_i$ ). (d) *pdf* of “diameter” of high enstrophy events in the streamwise direction in terms of  $\eta_i$

orientation (i.e. slicing through it perpendicularly all the way to slicing through it along its principal axis), the long tails are not surprising. The literature has often reported that the high enstrophy “worms” (Kerr 1985; Ashurst et al. 1987; Jiménez et al. 1993) have characteristic diameters of  $6\text{--}10\eta$ . Figure 5b shows that the *pdf* for the reference case DNS data has a clear peak at  $\approx 6.4\eta$ , which is in clear agreement with the literature. The *pdfs* for the lower resolution show this peak moving out as far as  $\approx 35\eta \approx 25\eta_i$  in the most coarsely resolved case. It is thus imperative to realise the effect that resolution plays in our ability to characterise these length scales. The effect of resolution on the length scales for these high enstrophy “worms” can be further visualised in Fig. 6. The increase in diameter in physical size can be visualised as resolution is decreased from Fig. 6a–d. The isosurfaces presented are for  $\omega_i^2$  equal to 1% of the global maximum of the relevant mean filtered dataset. This same trend is also observed in Fig. 7 which shows an identical perspective of isosurfaces of enstrophy, where  $\omega_i^2$  is again 1% of the global maximum for the relevant dataset, for the original experimental data (a) and the experimental data mean filtered at  $6\eta$  (b). In Fig. 6, the

contours in the background are of the magnitude of the velocity gradient tensor ( $|D_{ij}|$ ) and in Fig. 7, the contours are of dissipation. Both show the tendency for the extreme events to be filtered out as resolution is coarsened as previously discussed with reference to Fig. 3.

Even the most finely resolved mean filtered case,  $\Delta x = 2.5\eta$ , shows a slight tendency for the peak of the *pdf* of Fig. 5b to move to a value greater than  $6.4\eta$ . Ganapathisubramani et al. (2008) state that these structures can be observed to be up to  $40\eta$  in length based on a full-width of the structure at half the maximum value criteria. Indeed, Fig. 5b shows that the *pdf* for the reference DNS case has not quite reached zero at  $60\eta$ , suggesting that a small proportion of these “worms” can stretch to a much greater length than previously thought.

It should also be noted, by comparing Fig. 5a, b, that the length scales over which high dissipation events are spatially coherent are greater than those for enstrophy. This is due to the fact that high dissipation events are often found to occur in regions in which the intermediate strain-rate eigenvalue ( $s_2$ ) is positive (Ashurst et al. 1987). This leads to “sheet-forming” topology, whereas high enstrophy

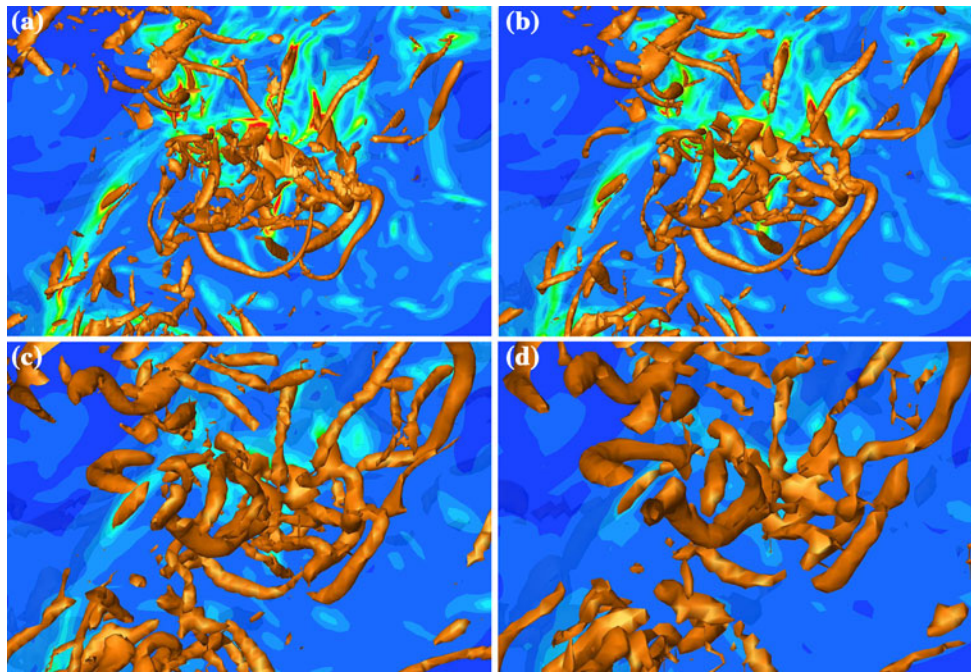


**Fig. 6** Isosurfaces of enstrophy ( $\omega_i^2$ ), where  $\omega_i^2$  is 1% of the global maximum for **a** the reference DNS case, **b** the dataset mean filtered at  $2.5\eta$ , **c** the dataset mean filtered at  $5\eta$  and **d** the dataset mean filtered at  $7.5\eta$ . Exactly the same region of the flow is illustrated from exactly

the same three-dimensional perspective in all four images. The contours in the background are magnitude of the velocity gradient tensor ( $|D_{ij}|$ ). It can be seen that as the spatial resolution decreases from **a** to **d** the extreme events of  $|D_{ij}|$  are filtered out

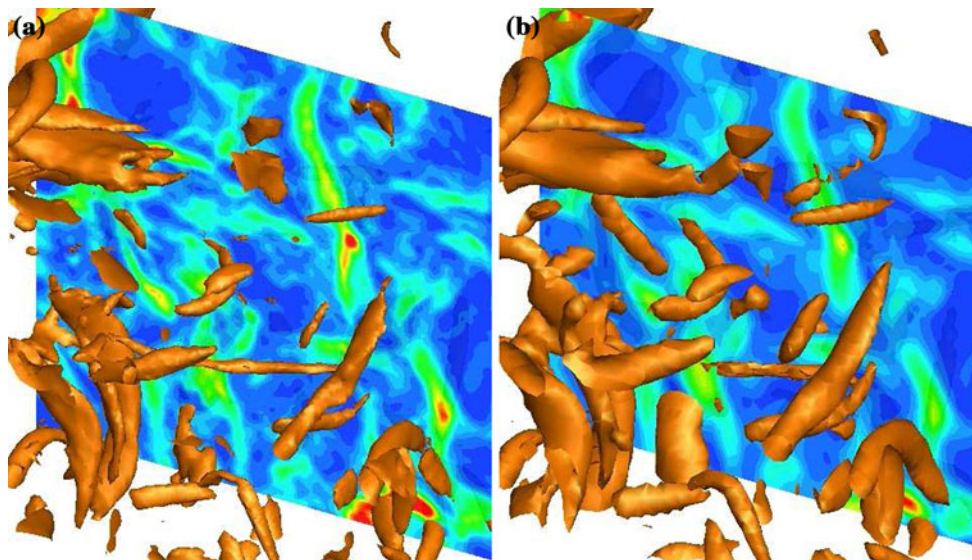


**Fig. 7** Isosurfaces of enstrophy ( $\omega_i^2$ ), where  $\omega_i^2$  is 1% of the global maximum for **a** the original experimental data, **b** the experimental data mean filtered at  $6\eta$ . Exactly the same region of the flow is illustrated from exactly the same three-dimensional perspective in

both images. The contours in the background are dissipation ( $\epsilon$ ). It can be seen that as the spatial resolution decreases from **a** to **b** the extreme events of  $\epsilon$  are filtered out

events are “tube-like” (“worms”). Sheets are spatially coherent over two dimensions, whereas tubes are only spatially coherent (over any great distance) in one. In addition, the peaks of Fig. 5a are at greater lengths than

those of Fig. 5b ( $r_\epsilon = 8.5\eta$  for the reference DNS case as opposed to  $r_{\omega_i^2} = 6.4\eta$ ). This suggests that strain-dominated regions of the flow are spatially coherent over greater distances than rotationally dominated regions. It would,

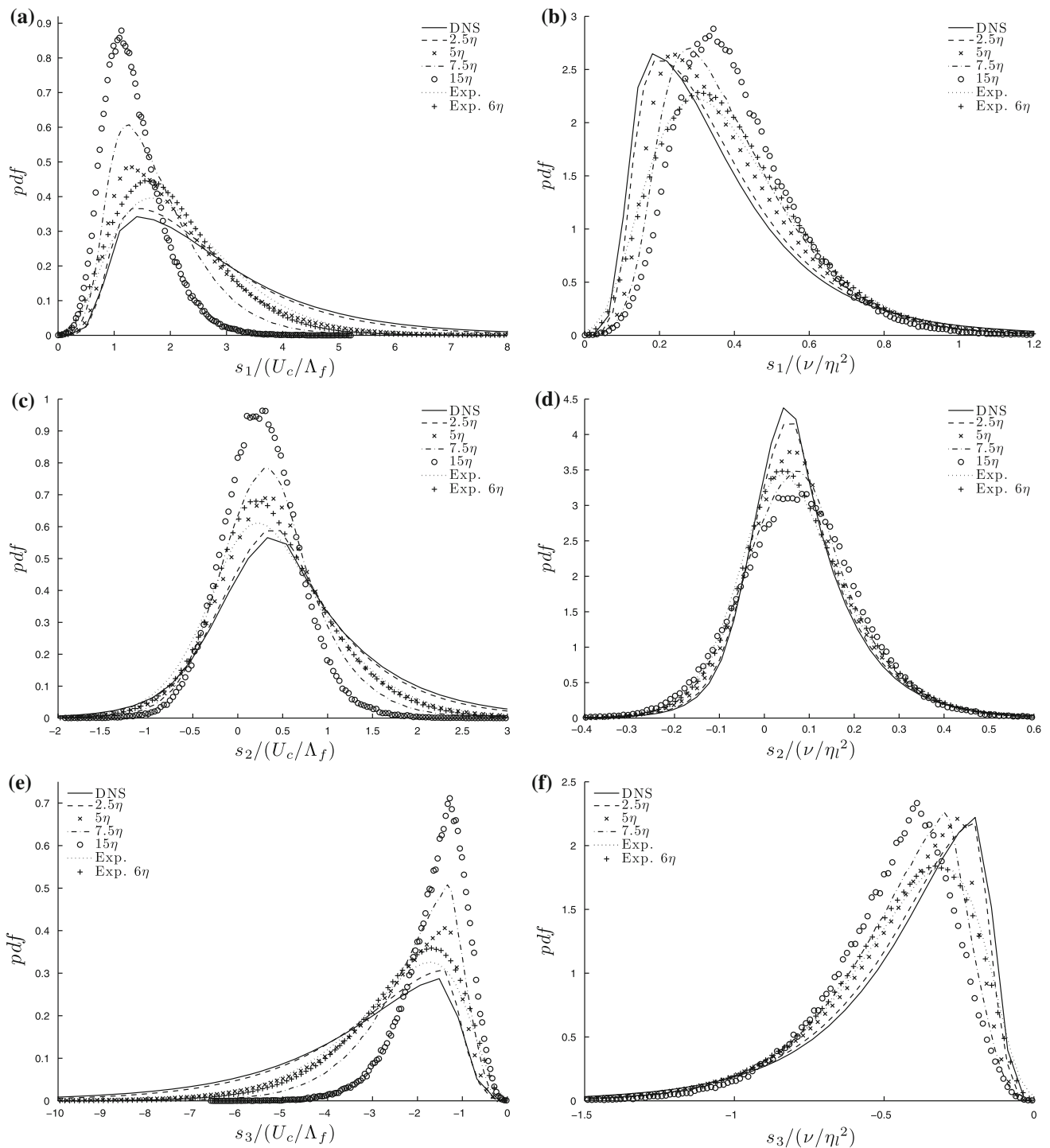


**Fig. 8** pdfs of eigenvalues of strain-rate tensor,  $s_i$ , normalised by large-scale quantities (left) and the local Kolmogorov length scale (right). Further explanation in the text

therefore, be expected that coarse resolution would have a disproportionately more severe effect upon the observation of rotationally dominated regions of the flow.

Figure 8 shows probability density functions for the eigenvalues of the strain-rate tensor for the reference DNS

dataset, the mean filtered datasets and the original and filtered experimental data. Figure 8a shows the pdfs for the extensive strain-rate eigenvalue ( $s_1$ ), (c) shows the intermediate strain-rate eigenvalue ( $s_2$ ), which can be either mildly extensive or compressive and is bounded by the

values of  $s_1$  and  $s_3$  and (e) shows the compressive strain-rate eigenvalue ( $s_3$ ) normalised by large-scale quantities. Measuring small-scale quantities experimentally is both challenging and dependent upon the resolution of the experiment, as illustrated by Table 1 and the movement of the *pdf* peaks from Fig. 5a, b to their values in Fig. 5c, d respectively.

Despite the fact that strain rates are fine-scale features, it is thus desirable to normalise them by large-scale quantities that are easier to measure and largely independent of the experiment's resolution. The quantity chosen is an inverse time scale formed as  $U_c/\Lambda_f$ , where  $U_c$  is a convection velocity and  $\Lambda_f$  is a large-scale vorticity thickness. For the numerical mixing layer,  $U_c$  is defined as  $(U_1 + U_2)/2$ , or the mean of the two free streams and for the experimental jet, it is defined as the mean streamwise velocity along the jet's axis. The vorticity thickness for the mixing layer is defined as  $\Lambda_f = (U_1 - U_2)/\left.\frac{\partial(u_1)}{\partial x_2}\right|_{\max}$  at the measurement location and as the jet half width at the measurement location for the jet flow. Figure 8(b), (d) and (f) show  $s_1$ ,  $s_2$  and  $s_3$  normalised by the "local" Kolmogorov length scale respectively.

The reduction in intermittency as resolution is coarsened is again clearly visible in the figures. It can be seen that for all three strain-rate eigenvalues, the tails of the *pdfs* are broader and, correspondingly, the peak values at the modal value are lowest at the most highly resolved of the numerical and experimental datasets and narrower and greater, respectively, at the coarsest resolution.

The large-scale normalised value at which the *pdfs* peak remains constant as resolution is coarsened for all three strain-rate eigenvalues. This suggests that the coarsening of resolution affects the extreme strain-rate events, at the tails of the *pdfs* and not the modal events. It can thus be deduced that the high magnitude strain-rates are spatially coherent over small distances and are thus "filtered out" at coarser resolution. This is in agreement with Ganapathisubramani et al. (2008) which showed that the large magnitude negative values of  $s_2$  are "spotty" and not spatially coherent over large distances and that high magnitude positive values of  $s_2$  are "sheet-like", with the thicknesses of these sheets being of the order of  $\approx 10\eta$ .

In contrast to the large-scale normalised *pdfs*, those that are normalised by the "local" Kolmogorov length scale show a variation in the location of the modal values. This effect is particularly pronounced for  $s_1$  and  $s_3$ . This again has serious implications for coarsely resolved experimental studies. The modal location of the strains remains unchanged for different resolutions when normalised by large-scale quantities or the true Kolmogorov scale of the flow. However, this feature will not be observed when the strains are normalised by dissipative quantities calculated

from the data, due to the variation of the Kolmogorov scale ( $\eta_l$ ) with resolution.

The experimental and numerical data both show a similar position for the peak location of the intermediate strain-rate at  $s_2 \approx 0.04 v/\eta_l^2$ . The intermediate strain-rate is responsible for determining the nature of the topological evolution of a fluid element. When  $s_2$  is positive, a fluid element is subjected to two orthogonal extensive strain-rates and a further compressive strain-rate in the third, orthogonal direction. This leads to the formation of "sheet-like" topology. In contrast when a fluid element is subjected to two orthogonal compressive strain-rates and a third orthogonal extensive strain-rate, i.e.  $s_2$  is negative, it will evolve into a "tube" or "worm-like" structure. The sign and magnitude of the intermediate strain-rate eigenvalue are thus of great physical significance to the topological evolution of a fluid element. Figure 8c, d show that there is a clear preference in shear flow turbulence, both from the experimental jet flow and the numerical mixing layer (at all spatial resolutions) for "sheet-forming" topological evolution over "tube-forming" topological evolution.

### 3.2 Effects of experimental noise and spatial resolution

The effect of noise on the kinematics of fine-scale turbulence is explored by adding random noise to the filtered DNS data. The noise is added such that the variance,  $\sigma$ , of the Gaussian function for all four spatial resolutions is identical. This means that the effects of resolution and noise can be separated out from each other. Evidently, the experimental data are subjected to a different degree of noise as well as being conducted at different spatial resolutions meaning that the separation of noise and resolution is not possible with the experimental data. Adding noise of a constant  $\sigma$  to the numerical data is also analogous to conducting experiments with the same equipment, i.e. the same cameras subjected to the same levels of noise, with the same PIV processing algorithm at different spatial resolutions, i.e. with lenses of different focal length or flows of different Reynolds numbers.

The level of noise present on an experimental dataset is dependent upon the technique and equipment used. For example, in a PIV experiment, a constant uncertainty of say 0.1 pixels per vector will be present in the measurement of the velocity field. This noise is assumed to be completely random, and hence can be modelled by the addition of Gaussian noise to the velocity fields of the numerical data. Gaussian noise of the same variance,  $\sigma = 4 \times 10^{-3}U_1$ , was thus added to the numerical datasets that had been mean filtered at the four different filter widths. This noise corresponds to a 0.4% uncertainty in the mean value of  $U_1$ , and a noise event of  $2\sigma$  will correspond to an error of 0.1 pixels if

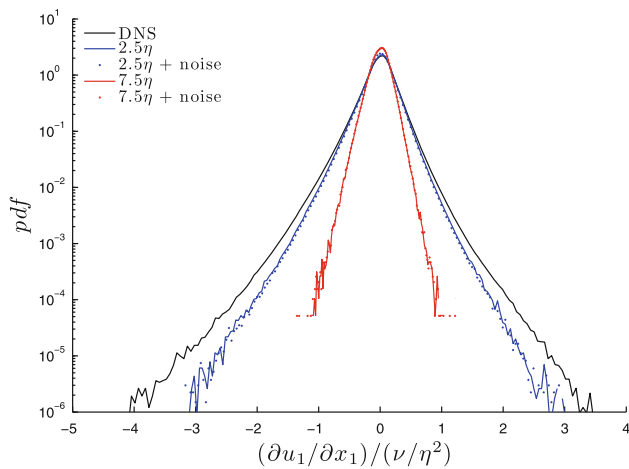


**Fig. 9** pdf for the  $\partial u_1/\partial x_1$  component of the velocity gradient tensor normalised by the Kolmogorov length scale from the reference case DNS (c.f. Fig. 1) for the reference case DNS and two of the numerical datasets, both with and without Gaussian noise added

the PIV experiment is tuned to a pixel displacement of 12.5 pixels for  $U_1$ , which is typical.

Figure 9 shows the pdfs for the  $\partial u_1/\partial x_1$  component of the velocity gradient tensor normalised by the reference case Kolmogorov length scale,  $\eta$ , as in Fig. 1. pdfs are shown for the reference case, and the datasets mean filtered at 2.5 and 7.5 $\eta$  both with and without Gaussian noise added. It can clearly be seen that the pdfs remain virtually identical for the cases to which noise has and has not been added. This is repeated in the pdfs for the other components of the velocity gradient, but is not shown for brevity. The tails of the pdfs are dominated by extreme events, which are highly intermittent, that can be up to several thousand times the mean value (Donzis et al. 2008). The effect of low variance Gaussian noise is thus of little significance to these extreme events and can only be seen in the less extreme “background events” which are not clearly

displayed in the semilog plot of Fig. 9 but are visible when the data are plotted on a linear ordinate axis which is not shown for brevity.

The importance of the intermediate strain-rate eigenvalue to the nature of the evolution of the topology of fluid elements within a flow has led to different ways of normalising it in order to investigate its tendencies. Ashurst et al. (1987) proposed normalising  $s_2$  as follows:

$$s_2^* = \frac{\sqrt{6}s_2}{\sqrt{s_1^2 + s_2^2 + s_3^2}} \tag{4}$$

where the denominator of Eq. 4 is equal to  $|S_{ij}|$ , the magnitude of the strain-rate tensor. For an incompressible flow  $s_2$  is bounded by  $\pm 1$ , with these extreme values corresponding to axisymmetric expansion and contraction, respectively. Figure 10a shows the pdf for  $s_2^*$  for the numerical data, the numerical data to which Gaussian noise has been added, the experimental data and the reference case DNS for comparison. The pdfs for the reference case DNS and the datasets mean filtered at 2.5 $\eta$  and 7.5 $\eta$  have the same modal value of  $s_2^*$ , as do those for the original experimental dataset and the one mean filtered at 6 $\eta$ . This suggests that the modal value for  $s_2^*$  remains constant regardless of spatial resolution. This value is again positive, emphasising the preference for “sheet-forming” for the evolution of fluid elements within the flow. The addition of Gaussian noise, however, reduces the magnitude of the pdf peak and moves it to a smaller  $s_2^*$  value for both the datasets mean filtered at 2.5 $\eta$  and 7.5 $\eta$ . There is a more distinct shift in the pdf peak for the dataset mean filtered at 2.5 $\eta$  when Gaussian noise is added than that mean filtered at 7.5 $\eta$ . Due to the effect of  $\Delta x$  increasing due to mean filtering this zero mean noise appears to have a lesser effect on the more coarsely resolved data.

The addition of Gaussian noise has the effect of introducing a divergence error into the data. This manifests

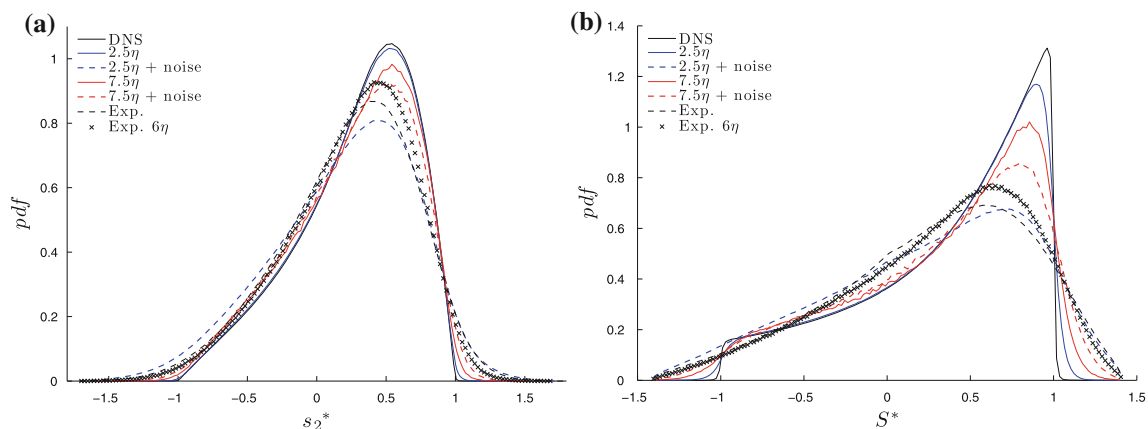


**Fig. 10** a pdf for  $s_2^*$  (defined in the text) from the numerical data, experimental data and numerical data to which Gaussian noise has been added. b pdf for  $S^*$  (defined in the text) from the numerical data, experimental data and numerical data to which Gaussian noise has been added

itself as the tails of the *pdfs* extending beyond  $s_2^* = \pm 1$  and the peak value of the *pdf* decreasing due to the extended range. This extension of the tails beyond  $s_2^* = \pm 1$  is also observed on the *pdfs* produced from the experimental data, highlighting the divergence error that is inherent in the data due to experimental noise. Further effects of this divergence error are discussed later.

Lund and Rogers (1994) argued that the normalisation of  $s_2$  in Eq. 4 does not capture the entire range of strain orientations uniquely and proposed a new normalisation:

$$S^* = \frac{-3\sqrt{6}s_1s_2s_3}{(s_1^2 + s_2^2 + s_3^2)^{3/2}} \quad (5)$$

This new normalisation is again bounded by  $S^* = \pm 1$ . Figure 10b shows probability density functions for  $S^*$  from the numerical data, the numerical data to which Gaussian noise has been added, the experimental data and the reference case DNS for comparison. A shift in the location of the modal value of  $S^*$  as resolution is decreased can be observed in the figure. This is predominantly due to the slight divergence error that is added to the data as the resolution is coarsened, illustrated by the extension of the tails of the *pdfs* from the data mean filtered at  $2.5\eta$  and  $7.5\eta$  extending beyond  $S^* = \pm 1$ . The *pdf* from the reference case, and to a lesser extent those from the coarser mean filtered datasets, show the characteristic shape presented in Lund and Rogers (1994). However, those created from the experimental datasets and the numerical datasets to which Gaussian noise has been added differ significantly, with the peak moving to a value of  $S^*$  somewhat less than one. This was also observed by Lund and Rogers (1994) when noise was added to their DNS data. The *pdfs* generated from the two experimental datasets can be seen to be both qualitatively and quantitatively similar to the noisy numerical datasets, with the tails extending some way past  $S^* = \pm 1$ . Ganapathisubramani et al. (2007) argued that this was due to a combination of experimental divergence error, caused by noise on the data, and a greater degree of uncertainty in lower magnitude velocity derivatives. It was showed, by means of joint probability density functions between velocity gradient tensor magnitude and  $S^*$  that this data were reliable, and comparable to DNS datasets at higher magnitudes of  $D_{ij}$ , such as those found in areas of high enstrophy/strain amplification rates.

Figures 10a, b show that experimental noise has a considerable effect on our observation of certain kinematic features of shear flow turbulence. One of the effects of this experimental noise is to add an artificial compressibility,  $\nabla \cdot \mathbf{u} \neq 0$ , to the data, highlighted by the extension of the tails of the *pdfs* of Fig. 10a, b beyond  $\pm 1$ .

Another kinematic feature of shear flow turbulence that is affected by this artificial compressibility is the

strain–rotation interaction. This interaction and the differences between rotation dominated and strain-dominated regions of the flow can be further examined by looking at the joint probability density functions between  $Q$  and  $R$ , the second and third invariants of the velocity gradient tensor respectively.

Figure 11 shows joint probability density functions between the second ( $Q$ ) and third ( $R$ ) invariants of the characteristic equation of the velocity gradient tensor for the numerical data normalised by large-scale quantities (a), the “local r.m.s. value of  $Q$ ” (b) and the experimental data and noisy numerical datasets (d). Figure 11c shows joint *pdfs* normalised by the large-scale quantity constructed from the dataset mean filtered at  $2.5\eta$  to which two different levels of noise have been added. The large-scale quantity used to normalise the *pdfs* of Fig. 11a, c is the same as that defined to normalise Fig. 8. The joint contour level for the *pdfs* of Fig. 11a, c is  $2 \times 10^{-3}$ , whereas those for (b) and (d) are both 1. The dashed lines mark  $D = 0$ , where  $D$  is the discriminant of the characteristic equation for the velocity gradient tensor of a divergence free flow and  $R = 0$ . The two sectors of the *pdf* for which  $D > 0$ , S1 and S4 in the terminology of Buxton and Ganapathisubramani (2010) are responsible for the bulk of the enstrophy attenuation (S1:  $D > 0$ ;  $R > 0$ ) and enstrophy amplification (S4:  $D > 0$ ;  $R < 0$ ). These two sectors are rotationally dominated regions of the flow ( $D > 0$ ). It can be seen in Fig. 11a that as the resolution decreases an increasing proportion of the data is found in these two sectors. Effectively, data are transferred from the strain-dominated regions for which  $D < 0$  to the rotationally dominated regions. In the reference case, DNS sectors S1 and S4 account for 21.3 and 31.3% of the total data points respectively, whereas in the dataset mean filtered at  $7.5\eta$  they account for 24.8 and 34.7% respectively. By contrast, the strain-dominated sectors S2 ( $D < 0$ ;  $R > 0$ ) and S3 ( $D < 0$ ;  $R < 0$ ) account for 36.4 and 11.0% of the reference DNS case respectively and 30.5 and 10.0% respectively of the dataset mean filtered at  $7.5\eta$ .

This effect, however, is not observed when the joint *pdfs* are normalised by the local r.m.s. value for  $Q$  ( $\sqrt{\langle Q^2 \rangle}$ ), as illustrated in Fig. 11b. The large-scale quantity used to normalise the *pdfs* of Fig. 11a is easy to measure experimentally and largely independent of the resolution of the experiment performed, whereas the r.m.s. value of  $Q$  changes (reduces) as the resolution of the experiment is coarsened due to the mean filtering effect illustrated in Figs. 1 and 2. The *pdfs* for all four resolutions show similar shapes thereby masking the fact that the flow is more rotationally dominated at larger length scales, and more strain dominated at shorter length scales.

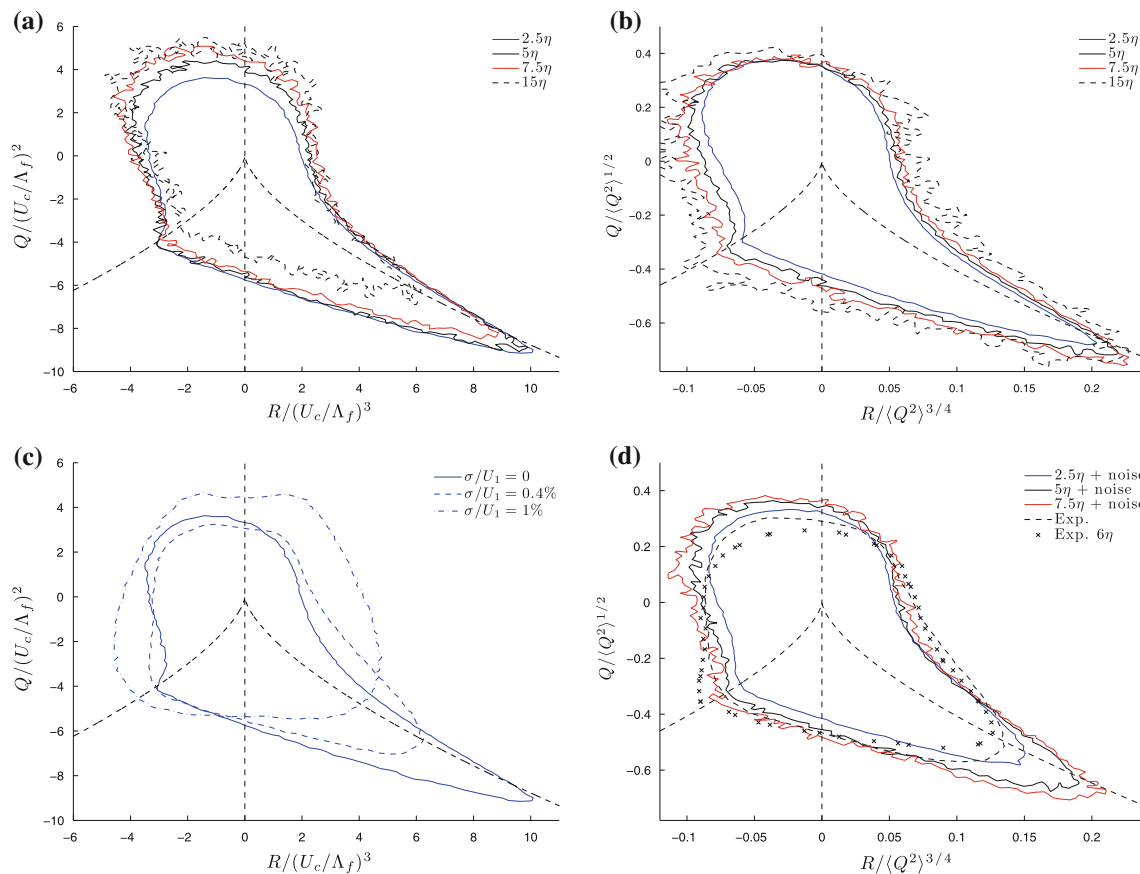


**Fig. 11** Joint probability density functions between  $Q$  and  $R$  **a** from the numerical datasets normalised by the large-scale quantity, **b** from the numerical datasets normalised by the local r.m.s. value of  $Q$  ( $\sqrt{\langle Q^2 \rangle}$ ) and **(d)** from the experimental datasets and the numerical datasets to which Gaussian noise has been added, normalised by  $\sqrt{\langle Q^2 \rangle}$ . **(c)** shows the effect of adding Gaussian noise of different

variances ( $\sigma$ ) to the dataset mean filtered at  $2.5\eta$ . The contours for **(a)** and **(c)** are at level joint pdf =  $2 \times 10^{-3}$  and for **(b)** and **(d)** are joint pdf = 1. The two dashed lines mark  $R = 0$  and  $D = 0$ , where  $D$  is the discriminant of the characteristic equation for the velocity gradient tensor in divergence free flow

This is of great importance to the experimentalist as the normalisation of these two important quantities by small-scale features, such as  $\eta_l$  (“local” Kolmogorov length scale) or  $\sqrt{\langle Q^2 \rangle}$  masks an important physical process. It is beneficial since the data at coarser resolution appear to have the same kinematic characteristics as that of finer resolution. Therefore, the effect of resolution can be factored out when normalised by the “local” values. The detrimental effect is that the normalisation with local values masks the fact that flow is more rotationally dominated for coarser resolution and more strain dominated at finer resolution. In order to reproduce the characteristic “tear-drop” shape of the  $Q - R$  joint pdf, it is thus recommended to filter the data to a coarser resolution, in agreement with Worth et al. (2010), and normalise by a large-scale flow quantity.

It can be observed from Fig. 11d that the joint pdfs produced from the experimental datasets are a different shape to those from the reference DNS dataset and the

literature (e.g. Chong et al. 1990; Perry and Chong 1994; Lüthi et al. (2009)). There is a significantly reduced strain-dominated “Vieillefosse tail” and a broadening of the rotationally dominated sectors S1 and S4 in the  $R$  direction, which is more pronounced for the coarsely mean filtered experimental dataset than for the original experimental dataset. This can be explained by the noise, inherent to the PIV process, that is present on the data. The first invariant of the characteristic equation for the velocity gradient tensor,  $P = \nabla \cdot \mathbf{u}$ , is not necessarily non-zero for the experimental data. This divergence error is in line with other similar experimental studies and is characterised and discussed further in Ganapathisubramani et al. (2007); however, it still plays an important role in shaping the  $Q - R$  joint pdf of Fig. 11. It can be shown that in  $P - Q - R$  space, the surface that separates purely real from complex roots, i.e. the discriminant in the three-dimensional space, can be given by (Chong et al. 1990):

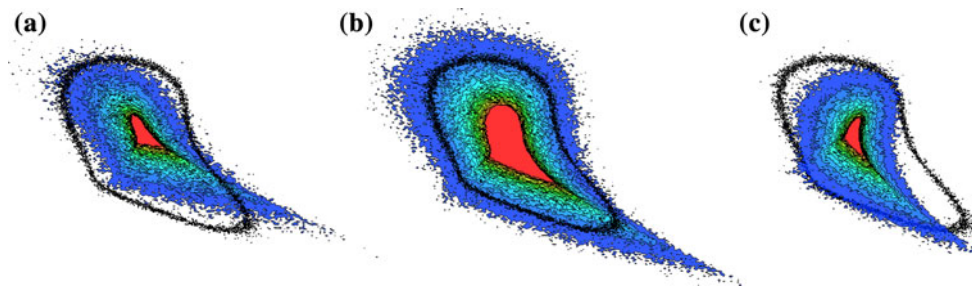


**Fig. 12** (a) Slice located at  $P/(v/\eta^2) = -0.25$  illustrating contours of the three-dimensional joint probability density function between  $P$ ,  $Q$  and  $R$  from the experimental dataset. (b) Slice located at  $P/(v/\eta^2) = 0$  for the three-dimensional joint  $pdf$ . The contour in *black*

represents the contour level of the joint  $pdf = 30$  of the experimental data of Fig. 11(d). (c) Slice located at  $P/(v/\eta^2) = 0.25$  for the three-dimensional joint  $pdf$

$$27R^2 + (4P^3 - 18PQ)R + (4Q^3 - P^2Q^2) = 0 \quad (6)$$

In fully divergence free flow ( $P = \nabla \cdot \mathbf{u} = 0$ ),  $D$  can thus be given by:

$$D = Q^3 + \frac{27}{4}R^2 \quad (7)$$

There is thus a discrepancy between the “surface” separating real from complex roots in the  $P - Q - R$  space of not fully divergence free data and the “ $D = 0$ ” condition separating them in fully divergence free data and illustrated as the dashed line in Fig. 11. A two-dimensional joint  $pdf$  thus becomes insufficient to characterise the flow according to the invariants of the velocity gradient tensor for a non-divergence free flow. The joint  $pdf$ s between  $Q$  and  $R$  generated from the noisy numerical datasets are also plotted on Fig. 11d. A similar “fattening” of sectors S1 and S4 and a diminishing of the strain amplification dominated “Vieillefosse tail” to the experimental datasets is observed for the noisy datasets, indicating that the Gaussian noise present in experimental data is responsible for the change in shape of the  $pdf$ s. Again it can be seen that as the resolution is coarsened the effect of the noise on the numerical datasets is decreased, as the joint  $pdf$ s for the data mean filtered at  $5\eta$  and  $7.5\eta$  to which Gaussian noise has been added look more similar in shape to those of Fig. 11a, b, with a more distinct “Vieillefosse tail”. The  $pdf$  from the numerical dataset mean filtered at  $2.5\eta$  to which noise has been added does, however, closely resemble the experimentally generated  $pdf$ s. This is also in agreement with the PTV study of turbulence under the influence of system rotation of Kinzel et al. (2010). Two spatial resolutions are used to produce joint  $pdf$ s between  $Q$  and  $R$ ,  $2.5\eta$  and  $9.5\eta$ . The study reports that as the resolution is coarsened the joint  $pdf$  loses its characteristic shape and more closely resembles that produced from a Gaussian field. Figure 11(c) shows that this is, however, a noise effect rather than a resolution effect. This figure shows  $pdf$ s produced from the dataset mean filtered at  $2.5\eta$  to which Gaussian

noise has been added with a variance of  $\sigma/U_1 = 0.4\%$  and  $\sigma/U_1 = 1\%$ . It can be seen that the shape of the  $pdf$  produced from the dataset to which the highest level of noise has been added is unrecognisable from those of Fig. 11(a), and closely resembles that of a Gaussian random variable and that of the coarsely resolved case in Kinzel et al. (2010). However, the joint  $pdf$  produced from the dataset mean filtered at  $15\eta$  ( $\approx 10\eta_i$ ) in Fig. 11(a) retains the characteristic “tear-drop” shape. Further joint  $pdf$ s were produced between  $Q$  and  $R$  for the more coarsely mean filtered datasets to which this higher level of noise has been added, but they are not shown for brevity. These confirm the finding that Gaussian noise has a diminishing effect on the shape of these  $pdf$ s as spatial resolution is coarsened. Equation 1 shows that as  $\Delta x$  is increased, i.e. resolution is coarsened, the velocity gradients decrease in magnitude. Thus, Gaussian noise of identical variance will reduce the magnitudes of the divergence error,  $\nabla \cdot \mathbf{u}$ , present on the data and hence the behaviour of the velocity gradient tensor’s invariants.

The effect of this Gaussian noise introduced divergence error on the experimental data is illustrated in figure 12. The figure shows three slices, located at  $P/(v/\eta^2) = -0.25$ ,  $0$  and  $0.25$  respectively of the three-dimensional joint probability density function between  $P$ ,  $Q$  and  $R$  for the experimental dataset with the two-dimensional  $Q - R$   $pdf$  of Fig. 11d superimposed as the black line. It can immediately be seen that the shape of the three-dimensional joint  $pdf$  at  $P = 0$ , i.e. where the divergence free criteria is met, is very similar to those of the numerical datasets of Fig. 11(a), with a clear “Vieillefosse tail” evident. Fig. 12(a) and (c) are presented to illustrate the effect of artificial compressibility, i.e.  $\nabla \cdot \mathbf{u} \neq 0$ , that is introduced into the data by means of intrinsic experimental errors. It can be seen that the three-dimensional  $pdf$  is not symmetric about  $P = 0$ , with regions of negative  $P$  tending to increase the contribution of sector S4 (relative to the divergence free case) and regions of positive  $P$  tending to increase the contribution of sector S1. Both  $P < 0$  and  $P > 0$  have the

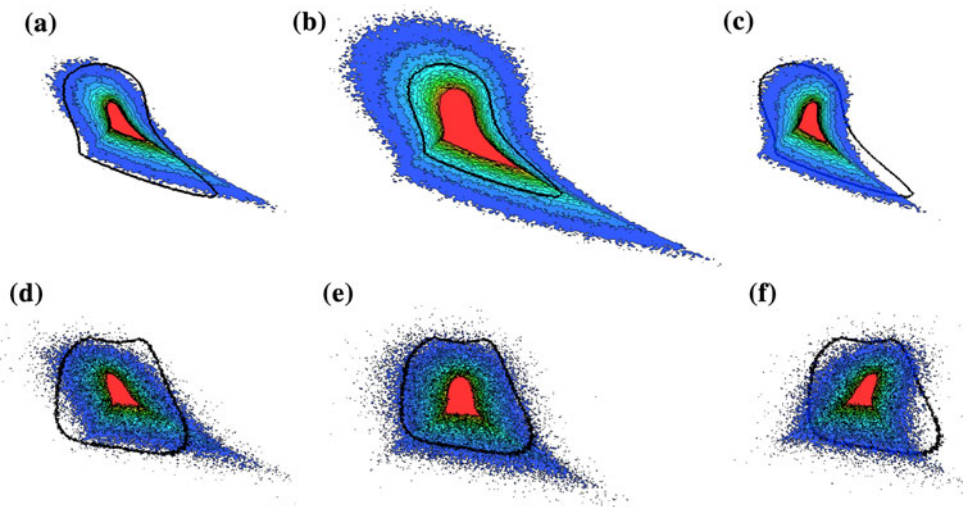


**Fig. 13** Slices located at  $P/(v\eta_1^2) = -0.15$  (a),  $P/(v\eta_1^2) = 0$  (b) and  $P/(v\eta_1^2) = 0.15$  (c) for the three-dimensional joint *pdf* between  $P$ ,  $Q$  and  $R$  for the numerical dataset mean filtered at  $2.5\eta$  to which Gaussian noise of variance  $\sigma/U_1 = 0.4\%$  has been added. (d), (e) and (f) show slices located at  $P/(v\eta_1^2) = -0.15$ ,  $P/(v\eta_1^2) = 0$  and  $P/(v\eta_1^2) = 0.15$  respectively for the  $P - Q - R$  3D joint *pdf* for the numerical dataset mean filtered at  $2.5\eta$  to which Gaussian noise of variance  $\sigma/U_1 = 1\%$  has been added. The contour in black represents the joint *pdfs* between  $Q$  and  $R$  from Fig. 11c for the two different noise levels

effect of reducing the “Vieillefosse tail”, with respect to the divergence free case, and thus the joint *pdf* between  $Q$  and  $R$  of Fig. 11 has a much greater proportion of swirling data points (sector S1 accounts for 29% and S4 accounts for 37% of the total data points).

The fact that the three-dimensional joint *pdf* is not symmetrical about  $P = 0$  is explained by the nature of the artificial compressibility “added” to the flow by the experimental error. When  $P$  is positive, i.e.  $\nabla \cdot \mathbf{u} > 0$ , this compressibility corresponds to a negative “density gradient” ( $\nabla \cdot \rho < 0$ ) which is representative of a compressible flow in a favourable pressure gradient in which waves travelling through the fluid diverge. When  $P$  is negative, this corresponds to a positive “density gradient” ( $\nabla \cdot \rho > 0$ ) which is representative of a compressible flow in an adverse pressure gradient in which waves travelling through the fluid coalesce (into a shock if the Mach number is greater than 1). These are thus two different physical processes and account for the asymmetry in the three-dimensional joint *pdf*. This is in agreement with the study of Pirozzoli and Grasso (2004), examining the effect of compressibility on turbulence. As spatial resolution is coarsened the divergence error of a dataset will increase since the dataset moves further away from the idealised “point measurement” for which the divergence free condition of an incompressible flow holds. This is also evident in the joint *pdfs* of Fig. 11(a) for the mean filtered datasets which show an increase in relative contributions of sectors S1 and S4 (relative the reference DNS case) and in Fig. 10. Three-dimensional joint *pdfs* between  $P$ ,  $Q$  and  $R$ , which are not shown for brevity, suggest that there is a slight

increase in the level of artificial compressibility introduced into these coarser datasets. This increases the relative importance of rotationally dominated regions of the flow, thereby increasing the distance over which these regions are spatially correlated, as visualised in Fig. 6.

The above observation is supported by the similar three-dimensional joint *pdf* between  $P$ ,  $Q$  and  $R$  of Fig. 13, formed from the well resolved ( $2.5\eta$ ) but noisy DNS dataset. Figure 13a–c again illustrate a slice of the joint *pdf* located at  $P/(v\eta_1^2) = -0.15$ , 0 and 0.15 respectively formed from the numerical dataset to which Gaussian noise of  $\sigma/U_1 = 0.4\%$  has been added. This again shows the “Vieillefosse tail” at  $P = 0$  and the relative increase in the importance of sector S4 for negative values of  $P$  and sector S1 for positive values of  $P$ . These same trends are also illustrated in Fig. 13d–f which show the three-dimensional joint *pdf* formed from the dataset mean filtered at  $2.5\eta$  to which the higher noise level of  $\sigma/U_1 = 1\%$  has been added, although it is obviously noisier. The artificial compressibility of experimental data thus increases the sector of  $Q - R$  space that is largely responsible for enstrophy amplification (S1) and reduces the contribution of the strain amplifying “Vieillefosse tail” thereby affecting the balance between these two terms which is of great importance to the dynamics of dissipation.

The interaction between strain and rotation is often examined by observation of the alignment between the eigenvectors of the strain-rate tensor and the vorticity vector. Figure 14 shows the *pdfs* for the magnitude of the alignment cosine between the vorticity vector and the extensive strain-rate eigenvector (a), intermediate

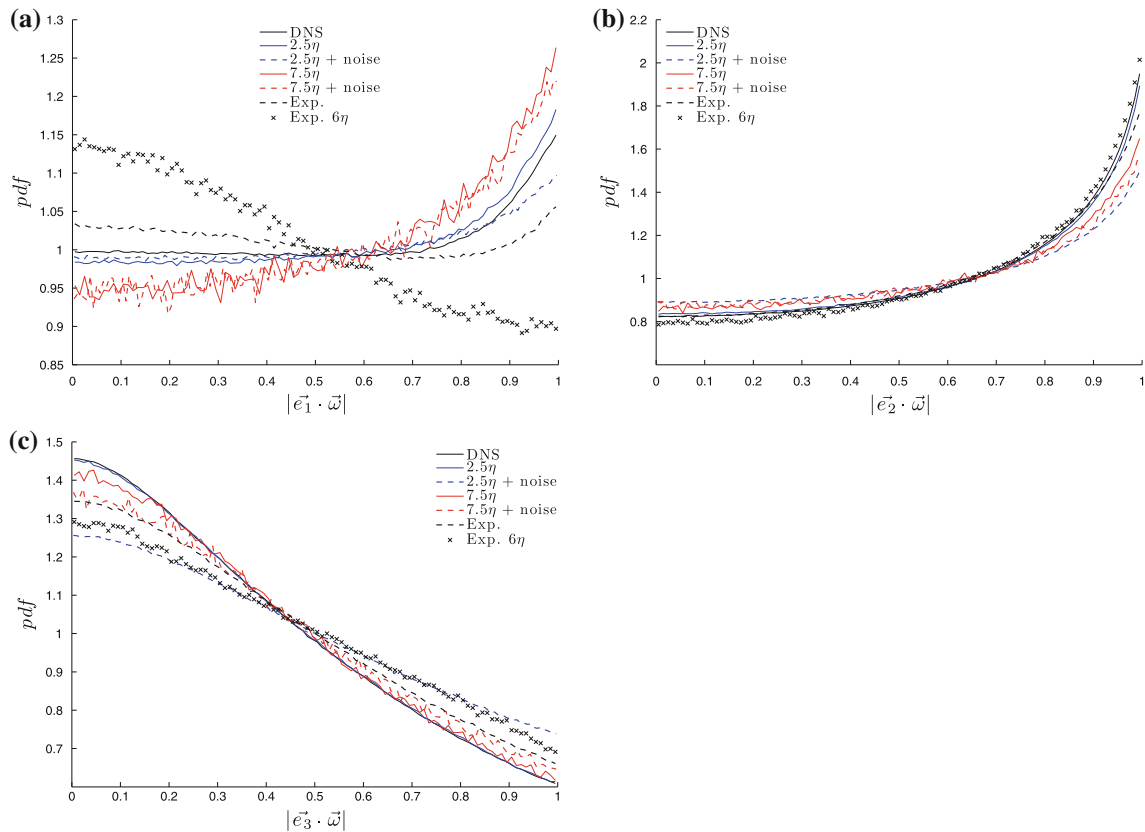


**Fig. 14** *pdfs* of magnitude of alignment cosine between the eigenframe of the strain-rate tensor (a) extensive eigenvector, (b) intermediate eigenvector and (c) compressive eigenvector and the

vorticity vector. The *pdfs* are constructed using the numerical datasets, numerical datasets to which Gaussian noise has been added and the experimental datasets

strain-rate eigenvector (b) and the compressive strain-rate eigenvector (c). All of the figures show *pdfs* produced from the numerical data, both with and without noise added and the experimental data with the reference case DNS also plotted for comparison. The *pdfs* from the reference case show the extensively reported arbitrary alignment between  $\vec{e}_1$  and  $\vec{w}$  and the preferential perpendicular  $\vec{e}_3 - \vec{w}$  and parallel  $\vec{e}_1 - \vec{w}$  alignments. There can be seen to be a slight resolution effect to the observation of these alignments. The datasets mean filtered at  $2.5\eta$  and  $7.5\eta$  show a slight tendency for  $\vec{e}_1$  to become aligned in parallel with  $\vec{w}$  as resolution is coarsened coupled to a slight reduction in the preference in parallel alignment between  $\vec{e}_2$  and  $\vec{w}$ .

There is no notable resolution effect to the alignment between  $\vec{e}_3$  and  $\vec{w}$ . The addition of Gaussian noise is observed to have a much more significant effect by observing the *pdfs* constructed from the mean filtered numerical datasets to which noise has been added. All three figures again show that the addition of noise is more significant to the more finely resolved ( $2.5\eta$ ) dataset than the coarser one ( $7.5\eta$ ). In general, noise can be seen to make the alignment between all three eigenvectors and  $\vec{w}$  more

arbitrary, i.e. “flatten” the *pdfs*. This does not appear to be the case for the experimental data, however. The fact that the addition of noise has a greater effect on the more finely resolved data is again a result of the amplification of the noise on the velocity field in the velocity gradients due to the smaller  $\Delta x$  in Eq. 1.

#### 4 Conclusions and further discussion

A direct numerical solution is performed for a nominally two-dimensional planar mixing layer and then mean filtered onto a regular Cartesian grid at four different spatial resolutions, namely  $2.5$ ,  $5$ ,  $7.5$ , and  $15\eta$ . This data, at different spatial resolutions, are then directly compared to the original DNS dataset and stereoscopic cinematographic PIV data from Ganapathisubramani et al. (2007) in order to examine the effect of spatial resolution on the kinematic fine-scale features that affect the strain–rotation interaction in shear flow turbulence. The experimental data are also mean filtered from an original resolution of  $3\eta$  to a new coarser resolution of  $6\eta$ .

The first important effect of reducing spatial resolution is the reduction of the magnitudes of the components of the velocity gradient tensor due to mean spatial filtering. The exponential tails to the *pdfs* of the components of  $D_{ij}$ , as reported by Sreenivasan and Antonia (1997), Ganapathisubramani et al. (2008) amongst others, are only visible at coarser resolutions of  $3\eta$  (the experimental resolution) and above. For the more finely resolved data, the gradients of these *pdfs* are not linear in semi-logarithmic coordinates but decrease at the high magnitude events. This spatial mean filtering has the effect of reducing the intermittency of the dissipation and enstrophy, the scalar analogues to strain and rotation respectively. Fine-scale turbulence is by its very nature an intermittent phenomenon and this intermittency has been shown to be extremely important to the rate of enstrophy amplification ( $\omega_i S_{ij} \omega_j$ ). “Extreme events”, those that are up to a thousand times the r.m.s. value and constitute the long tails of the *pdfs* such as Fig. 3, are responsible for a greatly disproportionate amount of the overall enstrophy amplification. It is found that coarser resolution has an almost equal effect on the reduction of intermittency of enstrophy (rotation) and dissipation (strain). This is despite the fact that dissipation is shown to be spatially coherent over greater length scales and in two dimensions as opposed to one; high enstrophy events are known to form “worms” (e.g. Jiménez et al. 1993) which are spatially coherent only in one dimension, whereas high dissipation events are known to form “sheets” which have a high spatial coherence in two dimensions.

In agreement with the experimental findings from the tomographic PIV study of Worth (2010), the length scale over which high dissipation events and high enstrophy events are spatially coherent is found to be a constant number of discrete grid points, regardless of the resolution of the grid. This suggests that the length scales of dissipation and enstrophy follow the filter that has been imposed upon them. This leads to these length scales becoming larger in physical units, as the resolution is coarsened. This is still the case, albeit to a lesser extent, when the characteristic length scales of these experiments are normalised by fine-scale quantities that are calculated from the data itself. Thus the growth of these structures as resolution is coarsened is diminished with respect to fine-scale flow quantities in comparison to fixed, large-scale quantities. Worth et al. (2010) suggested that the minimum resolution required to confidently determine these length scales is  $3\eta$ , the distance at which noise-related over prediction balances the spatial averaging under prediction of the spatial gradients. The comparison between the “best case” DNS and the data mean filtered at  $2.5\eta$  and the experimental data ( $3\eta$ ) suggests that even greater resolution may be required for a confident prediction. The fact that the experimental data of Fig. 3 falls between the DNS data

mean filtered at  $2.5\eta$ , and  $5\eta$  suggests that predictions as to the “real flow” may be made from under resolved data.

The eigenvalues of the rate of strain tensor,  $S_{ij}$ , determine the nature of the strain that a fluid element within the flow is subjected to. It has been shown that decreasing spatial resolution effects the extreme strain-rates far more than the more frequently occurring, modal events. The location of the peak/mode of the *pdfs* for all three principal strain-rates is observed to remain at the same location as resolution is decreased, in both the experimental jet flow and the numerical mixing layer, whereas the tails become narrower when normalised by large-scale quantities. This suggests that the extreme strain-rates are spatially coherent over only small distances, whereas the modal events are spatially coherent over much greater length scales. Again, however, when these quantities are normalised by fine-scale quantities calculated from the data itself there is a variance in the modal values of these strain-rates. Both the jet flow and mixing layer data show the same location for the modal value of the intermediate strain-rate eigenvalue at  $s_2 \approx 0.04\nu/\eta^2$ . This positive value reveals that shear flow turbulence has a preference for “sheet-forming”, as opposed to “tube-forming”, topological evolution of fluid elements as a positive intermediate strain-rate means a fluid element is subjected to two orthogonal extensive strains and a further orthogonal compression, resulting in a tendency to extend in-plane and flatten out of plane.

Another consequence of calculating spatial gradients from coarsely resolved data is that the divergence free condition ( $\nabla \cdot \mathbf{u} = 0$ ) vanishes and a divergence error is introduced into the data. This problem is exacerbated by noise introduced by experimental error (Ganapathisubramani et al. 2007). The effect of the introduction of a divergence error is to increase the importance of rotationally dominated regions of the flow, ones for which the characteristic equation for the velocity gradient tensor has complex roots, at the expense of the strain-dominated regions of the flow (real roots only). This is observed particularly in Fig. 12 which illustrates the effect of the artificial compressibility on the joint *pdf* between the second ( $Q$ ) and third ( $R$ ) invariants of the characteristic equation for the velocity gradient tensor generated from the original experimental dataset. This artificial compressibility is asymmetric about  $P = \nabla \cdot \mathbf{u} = 0$ , with  $P < 0$  increasing the relative contribution of sector S4 ( $D > 0$ ;  $R < 0$ ) and  $P > 0$  increasing the relative contribution of sector S1 ( $D > 0$ ;  $R > 0$ ). This behaviour is also observed in Fig. 13 which is generated from the numerical data to which Gaussian noise has been added to mirror the noise generated by the experimental process. Gaussian noise with a constant value of  $\sigma = 0.4\%$  of  $U_1$  was added to the numerical data at different spatial resolutions. It was observed that Gaussian noise has a decreasing effect on the

joint *pdfs* between  $Q$  and  $R$  as spatial resolution is coarsened, as a consequence of  $\Delta x$ , from Equation 1 increasing whilst  $\sqrt{\langle \mathbf{u}'_{\text{noise}}{}^2 \rangle}$  remains constant. An increase in the divergence error, either by the introduction of experimentally generated Gaussian noise or by a coarse spatial resolution also has a substantial effect on the dynamics of dissipation. The relative contribution of the strongly enstrophy amplifying sector  $S_4$  in  $Q$ – $R$  space is increased, whereas the strain amplifying “Vieillefosse tail” is diminished, thereby upsetting the balance of the source and sink terms for the dynamics of dissipation and skewing our observation of the strain–rotation interaction in shear flow turbulence.

A further distortion of our observation of the strain–rotation interaction due to the presence of experimental noise is also present in the alignment *pdfs* between the eigenvectors of the rate of strain tensor and the vorticity vector presented in Fig. 14. These show that there is a minor resolution effect in our observation of these alignments, the most important of which is the slight preference for  $\vec{\omega}$  to be aligned in parallel with  $\vec{e}_1$ , at the expense of  $\vec{e}_2$ . The effect of experimental noise is shown to be of greater significance than that of resolution. Noise is shown to make all three of the alignments more arbitrary and less pronounced.

**Acknowledgments** The authors would like to thank EPSRC for providing the computing resources on HECToR through the Resource Allocation Panel and for funding the experimental research through Grant No. EP/F056206. Funding from the Royal Aeronautical Society for ORHB is also greatly appreciated.

## References

- Antonia RA, Zhu Y, Kim J (1994) Corrections for spatial velocity derivatives in a turbulent shear flow. *Exp Fluids* 16:411–416
- Ashurst WT, Kerstein AR, Kerr RM, Gibson CH (1987) Alignment of vorticity and scalar gradient with strain rate in simulated Navier–Stokes turbulence. *Phys Fluids* 30:2343–2353
- Bermejo-Moreno I, Pullin DI, Horiuti K (2009) Geometry of enstrophy and dissipation, resolution effects and proximity issues in turbulence. *J Fluid Mech* 620:121–166
- Buxton ORH, Ganapathisubramani B (2010) Amplification of enstrophy in the far field of an axisymmetric turbulent jet. *J Fluid Mech* 651:483–502
- Chong MS, Perry AE, Cantwell BJ (1990) A general classification of three-dimensional flow fields. *Phys Fluids A* 2(5):765–777
- Christensen KT (2004) The influence of peak-locking errors on turbulence statistics computed from PIV ensembles. *Exp Fluids* 36:484–497
- Christensen KT, Adrian RJ (2002) Measurement of instantaneous Eulerian acceleration fields by particle image velocimetry: method and accuracy. *Exp Fluids* 33:759–769
- Donzis DA, Yeung PK, Sreenivasan KR (2008) Dissipation and enstrophy in isotropic turbulence: resolution effects and scaling in direct numerical simulations. *Phys Fluids* 20(045108):1–16
- Ganapathisubramani B, Lakshminarasimhan K, Clemens NT (2007) Determination of complete velocity gradient tensor by using cinematographic stereoscopic PIV in a turbulent jet. *Exp Fluids* 42:923–939
- Ganapathisubramani B, Lakshminarasimhan K, Clemens NT (2008) Investigation of three-dimensional structure of fine-scales in a turbulent jet by using cinematographic stereoscopic PIV. *J Fluid Mech* 598:141–175
- Ganapathisubramani B, Longmire EK, Marusic I, Pothos S (2005) Dual-plane PIV technique to determine the complete velocity gradient tensor in a turbulent boundary layer. *Exp Fluids* 39(2):222–231
- Herpin S, Wong CY, Stanislas M, Soria J (2008) Stereoscopic PIV measurements of a turbulent boundary layer with a large spatial dynamic range. *Exp Fluids* 45(4):745–763
- Jiménez J, Wray AA, Saffman PG, Rogallo RS (1993) The structure of intense vorticity in isotropic turbulence. *J Fluid Mech* 255:65–90
- Kerr RM (1985) Higher-order derivative correlations and the alignment of small-scale structures in isotropic numerical turbulence. *J Fluid Mech* 153:31–58
- Kinzel M, Wolf M, Holzner M, Lüthi B, Tropea C, Kinzelbach W (2010) Simultaneous two-scale 3D-PTV measurements in turbulence under the influence of system rotation. *Exp Fluids* 1–8. 10.1007/s00348-010-1026-6
- Laizet S, Lamballais E (2009) High-order compact schemes for incompressible flows: a simple and efficient method with quasi-spectral accuracy. *J Comp Phys* 228(16):5989–6015
- Laizet S, Lardeau S, Lamballais E (2010) Direct numerical simulation of a mixing layer downstream a thick splitter plate. *Phys Fluids* 22(015104):1–15
- Lavoie P, Avallone G, De Gregorio F, Romano GP, Antonia RA (2007) Spatial resolution of PIV for the measurement of turbulence. *Exp Fluids* 43(1):39–51
- Lund TS, Rogers MM (1994) An improved measure of strain state probability in turbulent flows. *Phys Fluids* 6(5):1838–1847
- Lüthi B, Holzner M, Tsinober A (2009) Expanding the  $Q$  –  $R$  space to three dimensions. *J Fluid Mech* 641:497–507
- Lüthi B, Tsinober A, Kinzelbach W (2005) Lagrangian measurement of vorticity dynamics in turbulent flow. *J Fluid Mech* 528:87–118
- Mullin JA, Dahm WJA (2006) Dual-plane stereo particle image velocimetry measurements of velocity gradient tensor fields in turbulent shear flow II. Experimental results. *Phys Fluids* 18(035102):1–28
- Perry AE, Chong MS (1994) Topology of flow patterns in vortex motions and turbulence. *Appl Sci Res* 53:357–374
- Pirozzoli S, Grasso F (2004) Direct numerical simulation of isotropic compressible turbulence: influence of compressibility on dynamics and structures. *Phys Fluids* 16(12):4386–4407
- Ruetsch GR, Maxey MR (1991) Small-scale features of vorticity and passive scalar fields in homogeneous isotropic turbulence. *Phys Fluids A* 3(6):1587–1597
- Sreenivasan KR, Antonia RA (1997) The phenomenology of small-scale turbulence. *Annu Rev Fluid Mech* 29:435–472
- Tao B, Katz J, Meneveau C (2000) Geometry and scale relationships in high Reynolds number turbulence determined from three-dimensional holographic velocimetry. *Phys Fluids* 12(5):941–944
- Tao B, Katz J, Meneveau C (2002) Statistical geometry of subgrid-scale stresses determined from holographic particle image velocimetry measurements. *J Fluid Mech* 457:35–78
- Taylor GI (1935) Statistical theory of turbulence. *Proc R Soc Lond A* 151(873):421–444
- Tennekes H, Lumley JL (1972) A first course in turbulence. MIT Press, Cambridge

- Tsinober A (1998) Is concentrated vorticity that important?. *Eur J Mech B/Fluids* 17(4):421–449
- Tsinober A, Kit E, Dracos T (1992) Experimental investigation of the field of velocity gradients in turbulent flows. *J Fluid Mech* 242:169–192
- van der Bos F, Tao B, Meneveau C, Katz J (2002) Effects of small-scale turbulent motions on the filtered velocity gradient tensor as deduced from holographic particle image velocimetry measurements. *Phys Fluids* 14(7):2456–2474
- Vieillefosse P (1982) Local interaction between vorticity and shear in a perfect incompressible fluid. *J Phys* 43(6):837–842
- Vincent A, Meneguzzi M (1994) The dynamics of vorticity tubes in homogeneous turbulence. *J Fluid Mech* 258:245–254
- Vukoslavčević P, Wallace JM, Balint JL (1991) The velocity and vorticity vector fields of a turbulent boundary layer. Part 1 (Simultaneous measurement by hot-wire anemometry). *J. Fluid Mech.* 228):25–51
- Wallace JM, Vukoslavčević P (2010) Measurement of the velocity gradient tensor in turbulent flows. *Annu Rev Fluid Mech* 42:157–181
- Westerweel J (2000) Theoretical analysis on the measurement precision in particle image velocimetry. *Exp Fluids [Suppl]* 29:S3–S12
- Worth NA (2010) Tomographic-PIV Measurement of Coherent Dissipation Scale Structures. Ph.D. thesis, Cambridge University
- Worth NA, Nickels TB, Swaminathan N (2010) A tomographic PIV resolution study based on homogeneous isotropic turbulence DNS data. *Exp Fluids* 49(3):637–656